Monolithic Sensor Integration in CMOS Technologies

Daniel Fernández, Piotr Michalik, Juan Valle, Saoni Banerji, Josep Maria Sánchez-Chiva, and Jordi Madrenas

***Abstract*—Besides being mainstream for mixed-signal electronics, CMOS technology can be used to integrate micro-electromechanical system (MEMS) on a single die, taking advantage of the structures and materials available in feature sizes around 180 nm. In this article, we demonstrate that the CMOS back-end-of-line (BEOL) layers can be postprocessed and be opportunistically used to create several kinds of MEMS sensors exhibiting good or even excellent performance, such as accelerometers, pressure sensors, and magnetometers. Despite the limitations of the available mechanical and material properties in CMOS technology, due to monolithic integration, these are compensated by the significant reduction of parasitics and system size. Furthermore, this work opens the path to create monolithic integrated multisensor (and even actuator) chips, including data fusion and intelligent processing.**

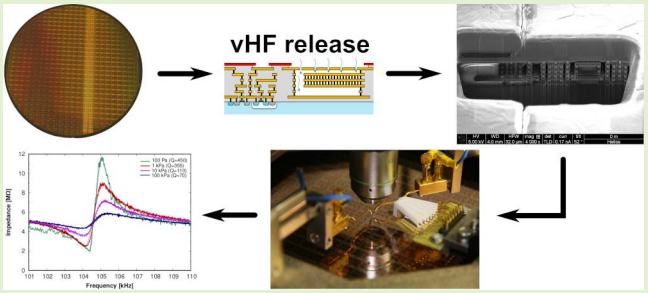

***Index Terms*—CMOS sensors, CMOS-micro-electromechanical system (MEMS), micromachining, monolithic integration, system-on-chip (SoC).**

I. Introduction

INTEGRATION is the key driving force in sensors for wearable applications. As wearable, human-interface devices (HIDs) shrink in space and increase in performance (from mobile phones to smart watches and from game pads to virtual-reality headsets), the market pull for more and more sensing and computing power in less and less printed circuit board (PCB) and silicon area grows stronger every day. Currently, any low-end smartphone endows an accelerometer, a gyroscope, a magnetic sensor, and more computing power than a full mainframe manufactured a few years ago. Also, all of them need to fit into the user's pocket. The problem becomes even worse if we think about smart glasses, watches, or rings. Many of them demand some computing power and also are orientation-aware or movement-sensitive to properly work. Hence, PCB area or package volume becomes the most valuable commodity, turning integration, from an important design consideration, into the key product-engineering factor.

Nowadays, bipolar-CMOS-DMOS (BCD) technologies allow us to pack the power converter, the microprocessor (μP), and any analog circuit all together on the same die, which is called system-on-chip (SoC) [1]. Certainly, this triggered the wearable revolution in which we live today. However, for the next step, serious consideration must be given to the sensor integration issue, which has been called the sensing SoC (SSoC) [2]. Sensors, such as accelerometers, gyroscopes, magnetic sensors, pressure sensors, and gas sensors, are designed to measure very specific physical magnitudes, and hence, they require very specific manufacturing processes; sometimes, incompatible between them. Some are not even manufactured as micro-electromechanical system (MEMS). In any case, usually, each sensor is manufactured in a single die, the sensor signal-conditioning and interfacing electronics in another die, and finally, the sensor fusion [3] algorithms in a third die or in the μP core. During packaging, the sensor die and the signal-conditioning die are wirebonded together and sealed inside the same package [4], [5], [6] in multichip modules (MCMs) or system-in-package (SiP) [1], whereas the sensor fusion μP is separately packaged. Although this is acceptable

Manuscript received 30 October 2022; revised 15 November 2022; accepted 23 November 2022. Date of publication 9 December 2022; date of current version 12 January 2023. This work was supported in part by Baolab Microsystems; in part by the Spanish Ministry of Science, Innovation and Universities (MCIN); in part by the State Research Agency (AEI); in part by the European Social Fund (ESF) under Project RTI2018-099766-B-I00; in part by MCIN/AEI/10.13039/501100011033 under Grant PID2021-123535OB-I00; and in part by ERDF, "A way of making Europe." The associate editor coordinating the review of this article and approving it for publication was Prof. Jean-Michel Redoute. *(Corresponding author: Daniel Fernández.)*

Daniel Fernández and Piotr Michalik are with Wiyo Technologies, 28109 Alcobendas, Spain (e-mail: daniel.fernandez@wiyotech.com; piotr.michalik@wiyotech.com).

Juan Valle, Josep Maria Sánchez-Chiva, and Jordi Madrenas are with the Department of Electronic Engineering, Universitat Politècnica de Catalunya, 08034 Barcelona, Spain (e-mail: juan.valle.fraga@gmail.com; jose.maria.sanchez.chiva@upc.edu; jordi.madrenas@upc.edu).

Saoni Banerji is with the Intelligent Materials and Systems Laboratory (IMS Laboratory), Institute of Technology, University of Tartu, 50411 Tartu, Estonia (e-mail: saoni.banerji@ut.ee).

Digital Object Identifier 10.1109/JSEN.2022.3224866

for the bigger wearables, such as smart phones (albeit not being a cost-effective solution), this is not the best option for the smaller, low-cost wearables we will have among us in the near future.

There are several techniques for achieving true monolithic integration (see [7], [8] for a comprehensive list), but in this article, we focus on what is called CMOS-MEMS back-end-of-line (BEOL) micromachining, that is, the use of the metallization interconnection layers of the CMOS process as structural layers for the MEMS device [9], [10], [11], [12], [13], [14]. In its simplest form [11], by just performing a release step, the silicon oxide surrounding the metallization interconnection layers is selectively removed, allowing the structures to move in response to external stimuli. This technique has the lowest cost and complexity among all options and has already shown its potential in high-yield, full-wafer scale, production environments [8], [15].

The manufacturing of all sensors and their electronics in the same silicon die has distinct advantages, as it can reduce area, package volume, and cost while improving the overall sensor performance. As a direct connection between the sensor and their electronics is possible, neither pads nor bonding wires are required between them; thus, noise and parasitics are greatly reduced. Also, the standard passivation of the CMOS process serves as a blocking layer for the release, so no additional masks are required, and as the release process can be done in batch volumes, the incremental cost of manufacturing MEMS in CMOS becomes very low. However, not all MEMS sensors are suitable for CMOS-MEMS BEOL monolithic integration: due to the low density and small thickness of the aluminum interconnections used as a structural material, sensors requiring a very high mass will find that the CMOS area footprint becomes too high, putting into question the cost advantages of the technique and risking having to face reliability issues caused by the inherent mechanical stress of the CMOS manufacturing process [16]. Other sensors requiring special materials or geometries may just find the CMOS manufacturing process incompatible.

Despite this, several device types can be fabricated using this technique, such as the accelerometers [17], [18], pressure sensors [19], [20], or magnetometers [15], [21]. MEMS RF switches have also been commercially produced by IHP foundry services [22], [23]. CMOS-MEMS mixers [24], filters [25], highly sensitive mass sensors [26], general-purpose resonators [27], and microbolometers [28] have also been reported. If we expand the concept of BEOL CMOS-MEMS to manufacturing processes requiring additional deposition of sensitive materials, a wider range of sensors can be designed. For example, a chemical sensor can be fabricated by depositing an absorbing material sensitive to a specific chemical over a resonator and then detecting its mass change [29], [30]. If we add piezoelectric materials to the manufacturing process, such as the SilTerra MEMS-on-Top PMUT MEMS process [31], we can build piezoelectric micromachined ultrasonic transducers (PMUTs) for applications such as fluid properties monitoring [32], micrometer-range distance measurements [33], or microimaging [34].

Due to the wide range of possibilities of BEOL-based CMOS-MEMS sensors and their huge economic potential, we will begin this article by presenting the manufacturing flow of the CMOS-MEMS sensors we designed over the last years, including their operation principle, device design, modeling, and measurements of some of our key sensors, namely, capacitive accelerometers, resonant Q-based pressure sensors, and Lorentz-force magnetometers, which form an interesting portfolio of CMOS-MEMS sensors and open the door to design monolithic multisensor devices. Specifically, after introducing the fabrication techniques of CMOS-MEMS sensors in Section II, we will present our accelerometer in Section III, our pressure sensor in Section IV, and our magnetometer in Section V, whose combination allows the implementation of monolithic SSoC. We will finish this article by presenting our views on the future of CMOS-MEMS in Section VI.

II. Fabrication of BEOL-Based CMOS-MEMS Sensors

In our designs, we used two CMOS processes, the IHP SG25 0.25-μm five-metal process for the accelerometer and pressure sensor presented in Sections III and IV, respectively, and the GlobalFoundries 0.18-μm ULL six-metal process for the magnetometer presented in Section V. The accelerometer and the pressure sensor were manufactured together in the same die, while the magnetometer was manufactured separately. In all cases, each sensor has its corresponding front-end electronics manufactured monolithically in the same die as the sensor. The metallization of both processes consists of several layers of aluminum separated and isolated by silicon dioxide and electrically connected by tungsten vias. In these technologies, a chemical–mechanical polishing (CMP) of the wafer is performed after each layer deposition, so they are not conformal. Layer thicknesses depend on each process, ranging from 0.5 μm of GlobalFoundries Metal 1 to 3 μm of IHP Metal 5. In Fig. 1, the process cross section for the GlobalFoundries process is shown, whereas one of the IHP processes is available in [13].

After the foundry manufactures the wafer, a release agent consisting of hydrofluoric (HF) acid in either liquid [11] or gaseous state [35] was applied to the wafers (see Fig. 2). Although some CMOS foundries have the machines necessary for performing a gaseous-state release, an approved manufacturing process flow is usually necessary to perform the release inside the CMOS foundry, so we used instead our own cleanroom for doing the liquid release and the *Memsstar* and *SPTS Primaxx* facilities for the gaseous-state release.

The passivation layer, a composite of silicon nitride (Si_3N_4) used to protect the electronics, was also used as a release mask. The release agent was only able to remove the silicon dioxide unprotected by the passivation openings, and hence, the electronics did not suffer any damage. For additional protection, a release cavity enclosure, made of via and metal, was designed and placed below the MEMS passivation opening to contain the release. This concept of release cavity enclosure can also be used to design structural MEMS parts with unreleased silicon dioxide within, allowing for the design of electrically isolated sensor components [15], [21] or

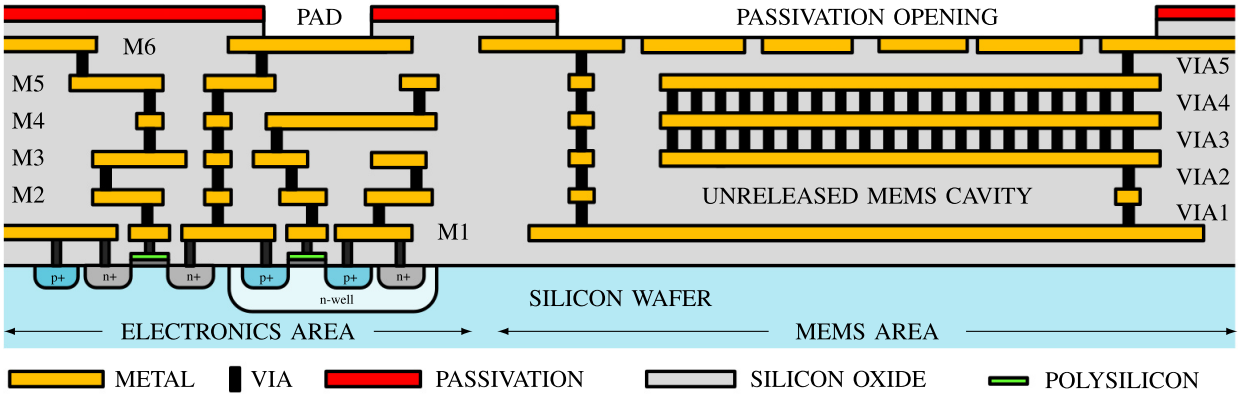

Fig. 1. GlobalFoundries 0.18-μm ULL process cross section before the release. Left: we can see the microelectronics section. Right: MEMS sensor section.

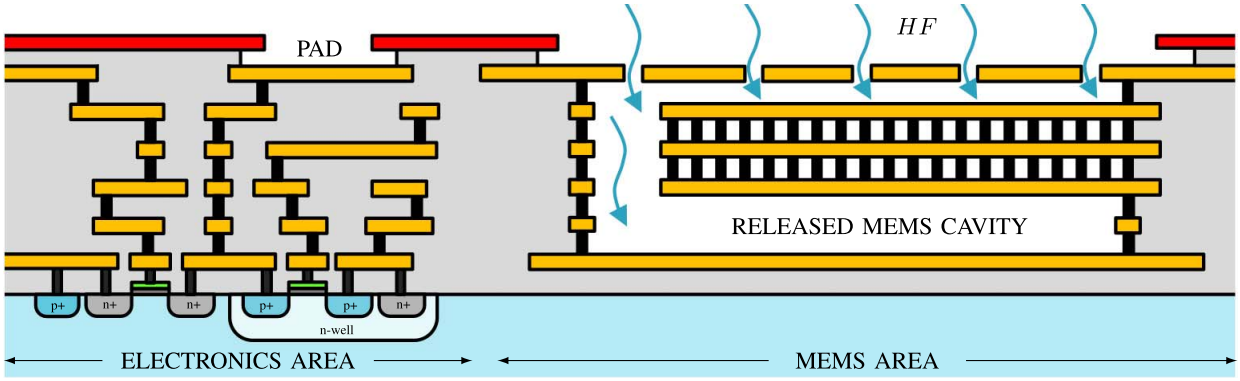

Fig. 2. GlobalFoundries 0.18-μm ULL process cross section after release, but before sealing. The HF-based release agent enters the MEMS cavity through the uncovered Metal 6 holes in the MEMS section and removes the oxide inside the MEMS cavity.

stress-compensated structures [16]. Also, around the passivation openings, a barrier made of the top metal was drawn between the openings and the electronics to limit the effect of the release outside the cavity. This underetching barrier has to overlap the underetching distance in order to be effective. We observed an underetching distance between 10 and 15 μm for the time needed to release all structures, so safe distances between 15 and 20 μm are sufficient to contain the release (see Fig. 4). Beware, however, that underetching also occurs in the pad passivation openings, not just in the MEMS passivation openings, so the top metal in the pads needs also to be extended in order to maintain the wirebonding reliability. Alternatively, with a modest increase in process complexity and cost, it is possible to protect the pads with some resistance before the release and then remove it afterward.

For the devices requiring low pressure or a controlled atmosphere to operate, a sealing made of aluminum and deposited using sputtering [36] was made. The sputtering parameters were carefully controlled to be able to perfectly cover the release holes and seal the devices. For convenience, the sputtering was also applied to the pad openings, thus providing an additional thickness to the pad metal and a more relaxed specification on the pad underetching distance, as the sputtered aluminum improves the pad mechanical reliability during wirebonding. Cross section in Fig. 1 after the release and sealing steps is shown in Figs. 2 and 3, respectively. A standard, low-cost plastic-molding packaging was also tested for this application, specifically SOP20 for the development devices and a quad flat no-lead (QFN) 16-pin 4 $\times$ 4 mm for the production devices. Neither of them shows a significant yield nor performance loss after packaging or soldering.

Focused-ion beam (FIB) cuts were done on the wafer and images were taken using a scanning electron microscope (SEM) at each step of the process in order to confirm the feasibility of the approach, as shown in Fig. 4. The images show that the release has removed the oxide inside the cavity (see black surfaces in the cut) and also that the sealing covered the release holes perfectly. The pressure inside the cavity was estimated to be below 200 µbar after sealing and about 2.5 mbar after a high-temperature storage (HTS) JESD22-A103D test (consisting on 1100 h storage at 150 °C) was performed. MSL1 and MSL3 tests, as well as the JEDEC JESD22-A104D temperature cycling test (consisting of 500 cycles between 150 °C and −65 °C), did not reveal any significant pressure increase.

Despite that the CMOS process is not an MEMS process, our analysis of more than 100 full wafers in ten different runs on four different foundries using 0.5-, 0.25-, 0.18-, and 0.15-μm CMOS process nodes [8] shows that there is an excellent mechanical repeatability among wafers [16], [35], demonstrating that volume production is feasible, reaching a 95% yield even after standard plastic-molded packaging.

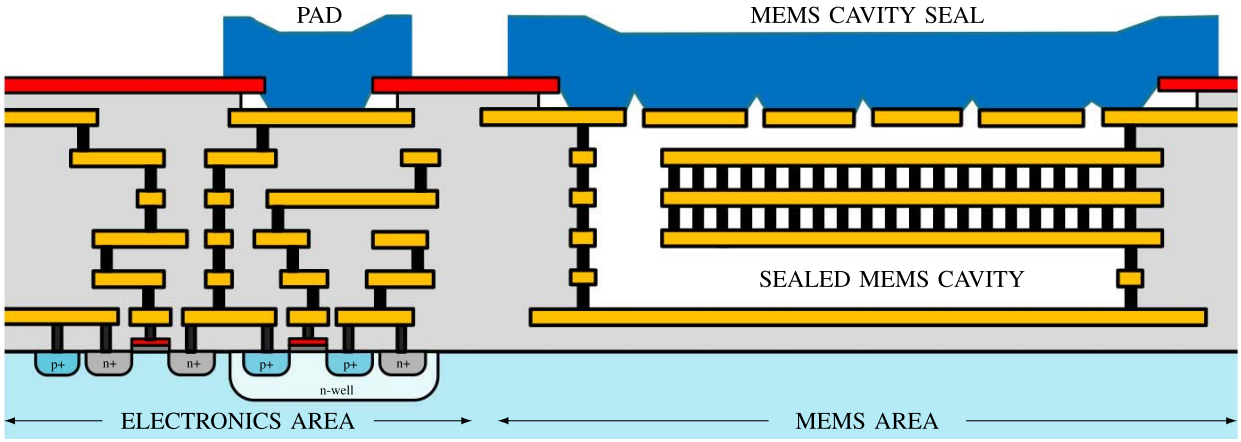

Fig. 3. GlobalFoundries 0.18-μm ULL process cross section after the release and the sealing with aluminum sputtering. The MEMS section is now protected from external agents and the wafer can be handled like a regular CMOS wafer.

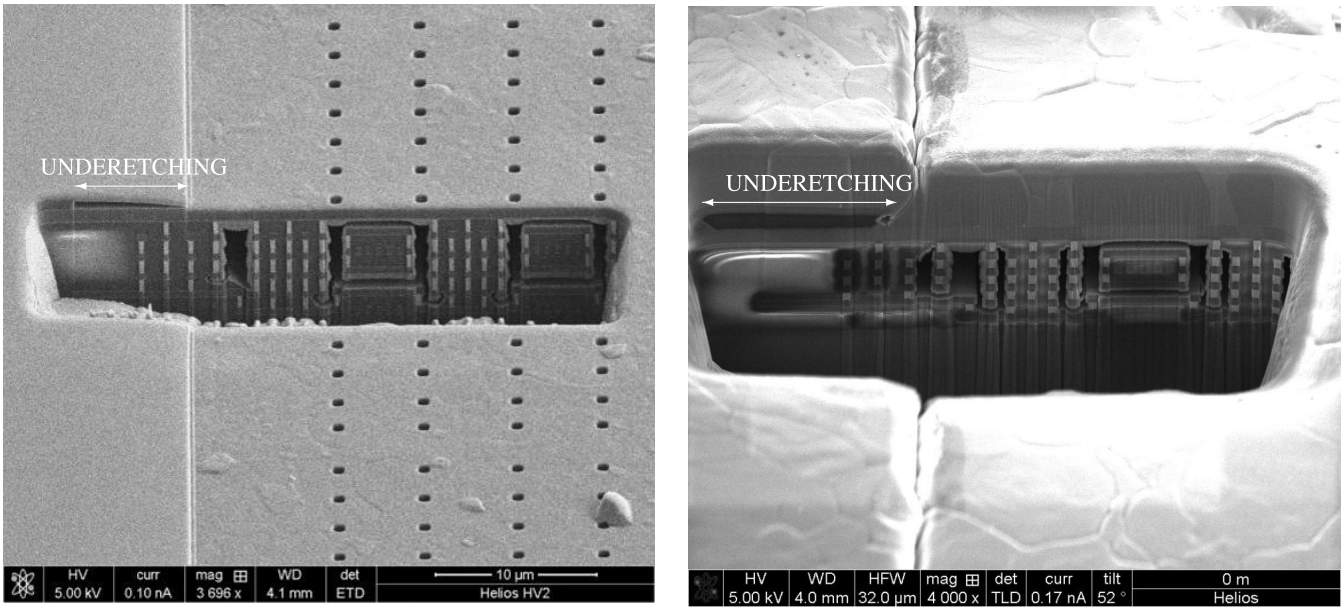

(a) (b)

Fig. 4. SEM images taken over FIB cuts of an in-plane (*XY* axes) CMOS-MEMS magnetometer taken (a) after release but before sealing and (b) after release and sealing. Note the perfect coverage of the release holes on Metal 6 after sealing and the underetching effect below the passivation. Note also the release cavity enclosure barrier preventing the release agent from etching the rest of the die and also some selected parts of the sensor.

III. Accelerometers

Accelerometers commonly work by detecting the inertial movement of a proof mass anchored to a frame of reference (the wafer, in our case). The intrinsic sensitivity of the accelerometer—that is, how much the proof mass moves when subjected to an acceleration—only depends on the ratio between the mass of the released structure and the stiffness of the suspensions anchoring it to the wafer. Increasing the mass implies increasing area or volume, and decreasing the stiffness of the suspensions severely affects the reliability of the device. Hence, a significant effort has been done to improve the sensing techniques with the objective of extracting the maximum acceleration information out of the same device. Among those techniques, the following conditions hold:

1) piezoresistive sensing [37], in which the movement of the proof mass is detected by the change of electrical resistance of a piezoresistive material attached to a suspension;
2) resonant sensing [38], [39], in which the proof mass works as a frequency-tuning element in an oscillator;
3) tunneling sensing [40], in which the tunneling current through nanometer gap between a proof mass and sharp electrode is detected;
4) thermal sensing [41], in which the moving element is a tiny bubble of heated air sealed in the sensor package cavity and its position is sensed using thermocouples;
5) capacitive sensing [42], in which the movement is detected by sensing the capacitance between a movable

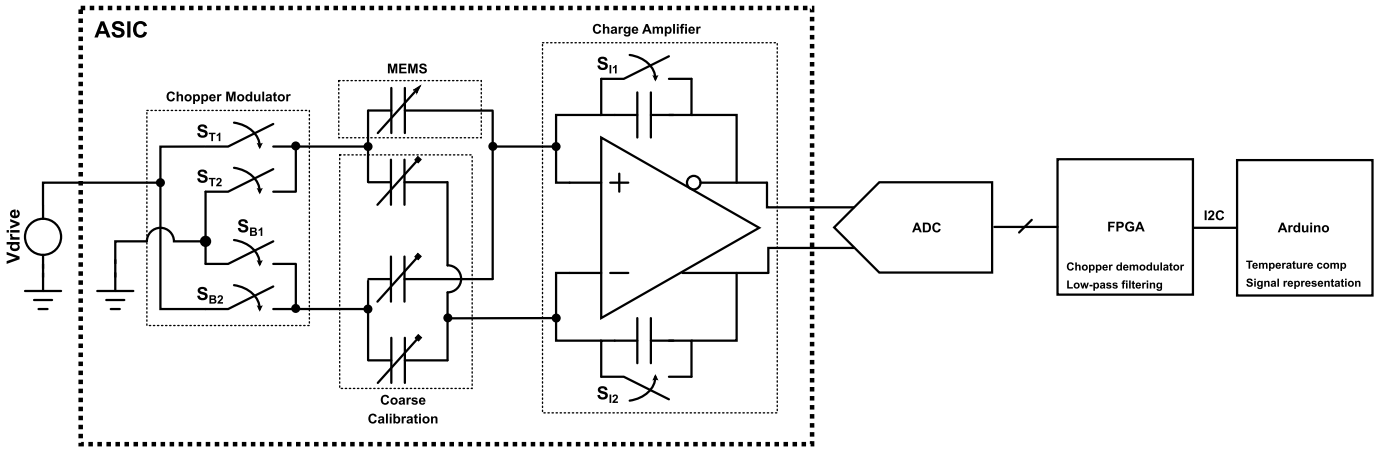

Fig. 5. Architecture and design partitioning of the accelerometer sensing electronics. The bigger dash square contains the monolithically integrated MEMS and sensor front end, while the small ones represent the individual ASIC functional blocks.

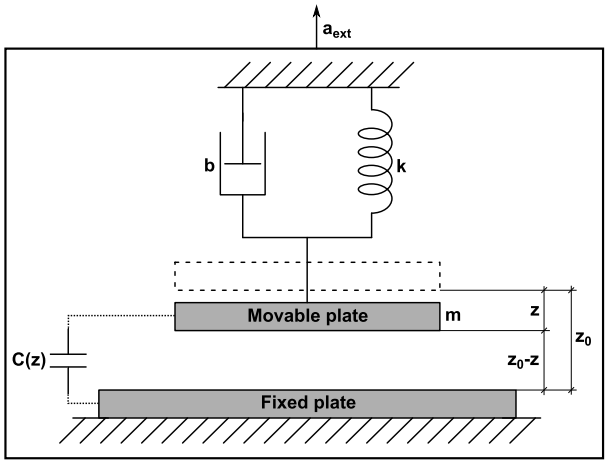

Fig. 6. Lumped-element model of a *z*-axis two-plate capacitive MEMS accelerometer.

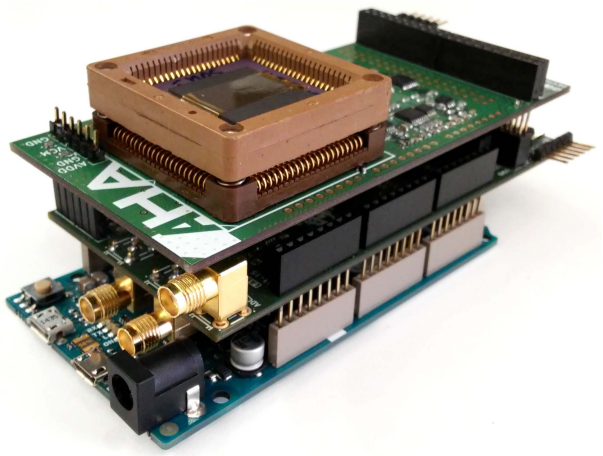

Fig. 7. CMOS-MEMS accelerometer prototype setup. Top: PCB with the analog signal-conditioning electronics and the ASIC. Middle: GA PCB that executes the digital signal processing algorithms. Bottom: Arduino Due board with the communications and the signal correction functions.

electrode attached to the proof mass and a fixed electrode attached to the wafer.

Nowadays, capacitive sensing is the most ubiquitous sensing approach for acceleration sensors. Its main advantages are no dc power dissipation by the sensing element, good temperature, and long-term drift stability and high bandwidth. This is the sensing technique used in the device here presented.

A. Device Modeling

An MEMS accelerometer is most commonly modeled as a lumped-element second-order mass–spring–damper system, as shown in Fig. 6. It follows the well-known second-order differential equation:

$$ma_{\text{ext}} = m\frac{d^2z}{dt^2} + b\frac{dz}{dt} + kz \tag{1}$$

where m is the proof mass, a_{ext} is the external acceleration, z is the displacement of the proof mass, b is the damping coefficient, and k is the spring constant.

For the frequencies below the device natural frequency ω_0, the displacement of the proof mass is proportional to the acceleration to be measured

$$z = a_{\text{ext}}\frac{m}{k} = \frac{a_{\text{ext}}}{\omega_0}. \tag{2}$$

Using capacitive sensing, the device capacitance can be approximated using a parallel-plate capacitor model in which the gap of the capacitor directly relates to the displacement and the acceleration

$$C\left(a_{\text{ext}}\right) \approx \frac{\varepsilon_0 A}{z_0 - z\left(a_{\text{ext}}\right)} = \frac{\varepsilon_0 A}{z_0 - \frac{a_{\text{ext}}}{\omega_0}} \tag{3}$$

where A is the capacitor area, ε_0 is the permittivity of a medium between the plates (air by default), and z_0 is the on-rest gap. As the displacement $z(a_{\text{ext}})$ is small in comparison to the z_0 gap, the previous equation can be approximated using a Taylor series by

$$C\left(a_{\text{ext}}\right) \approx \frac{\varepsilon_0 A}{z_0}\left(1 + \frac{a_{\text{ext}}}{z_0\omega_0}\right) + O\left(a_{\text{ext}}^2\right) \tag{4}$$

where we can see that the capacitance is incrementally linear with the acceleration. Equation (1) together with

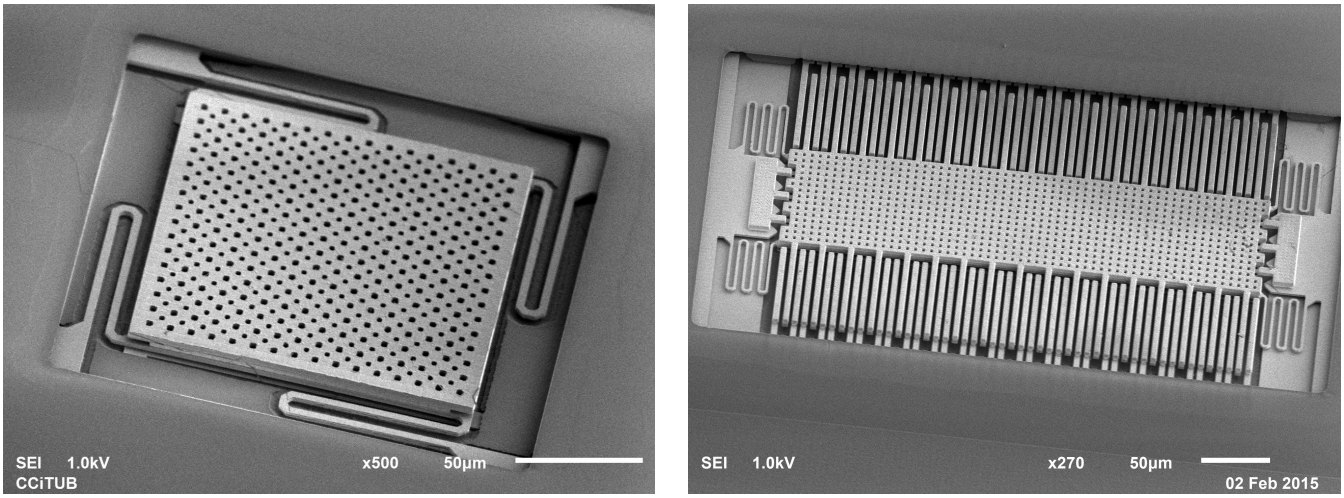

(a) (b)

Fig. 8. SEM images of (a) out-of-plane axis sensor and (b) in-plane axes.

the parallel-plate capacitor equation was implemented in a Verilog-A model to allow for a dynamic co-simulation of the MEMS sensor and the sensing electronics inside the Cadence Design Suite.

B. Device Design

For the accelerometer, two devices were designed and measured: one sensitive to the vertical acceleration (out-of-plane axis) and another for the horizontal acceleration (in-plane axes). Both were manufactured using the IHP SG25 0.25-μm five-metal process. A wet-etch release using HF acid in liquid form [11] was used to remove the oxide and release the proof mass. Also, to reduce the stiction, the dies were rinsed in methanol and dried in an oven after the release.

The front-end electronics and the temperature sensor were implemented monolithically with the sensor to maximize the performance, whereas the rest of the signal processing chain was implemented using discrete components to speed up the design cycle, as shown in Fig. 5. The sensing architecture for both accelerometers is based on a chopper-based charge-sensitive amplifier with a programmable capacitor for coarse calibration. Chopper demodulation and filtering take place in a discrete FPGA and temperature corrections in a μP Arduino Due board. A photograph of the whole prototype setup, including the MEMS die, can be seen in Fig. 7.

1) Out-of-Plane Axis: A square plate of 150 $\times$ 150 μm composed of the two top thick metals Metals 4 and 5 of 2 and 3 μm, respectively, as well as the 3-μm-tall via in between, was used as a proof mass [18]. Four U-shaped suspensions were attached at the corners using only the Metal 4 layer. The sensor presents a 0.6-μg mass, a single-ended sensing capacitance in the range of 50 fF, a sensitivity of 14 aF/G ($G \approx 9.81$ m/s^2), and a 20-kHz mechanical resonance. Its SEM microphotograph can be seen in Fig. 8(a).

2) In-Plane Axes: The sensor is a classic comb-type structure with a total size of 500 $\times$ 360 μm, composed also of the two top thick metals Metals 4 and 5 as the out-of-plane axis device [17]. The proof mass is suspended by four sixfold 2-μm-thick Metal 4 serpentine springs of 2 μm width and 45 μm length. The fingers overlap by 75 μm and are separated by 2.5 μm. The sensor presents a 1.95 μg mass and differential-sensing capacitance in the range of 2 $\times$ 80 fF, a sensitivity of 200 aF/G, and a 7.4-kHz mechanical resonance. Its SEM microphotograph can be seen in Fig. 8(b).

C. Measurements and Results

1) Out-of-Plane Axis: In Fig. 9, the linearity and temperature behavior of the out-of-plane axis accelerometer is shown. The device shows an excellent linearity on the selected range, making unnecessary to implement lookup tables for linearization in the digital domain. The temperature behavior, on the other hand, shows a very big dependence with temperature, in the order of 8.25 G/°C. Finite-element method (FEM) simulations indicated that this is due to the deformation of the movable plate with temperature, a phenomenon that can be mitigated with a multiple-electrode differential-sensing approach and adequate positioning of the plate anchors [43].

The accelerometer was also tested by measuring its noise floor over the full spectrum by performing a fast Fourier transform (FFT) analysis of its output without applying any acceleration, as well as measuring its spectral purity by applying a 30-Hz acceleration stimuli using a vibrating plate [see Fig. 10(a)]. The measured noise floor was 1.5 mG/(Hz)$^{1/2}$ at 30 Hz and the total root-mean-square (rms) noise was 18 mG over the bandwidth from 0.25 to 100 Hz. Better noise figures can be obtained by placing the sensor in vacuum to reduce the Brownian noise, increasing the power consumption to reduce the electronics noise, or simply increasing the sensor mass to reduce the impact of both. For a given MEMS sensor specification and system constraints, electronics noise can be minimized following the approach given in [44].

Experiments also show that our accelerometer generated far lesser frequency spurs than the commercial reference device. Also, both long- and short-term stabilities were measured

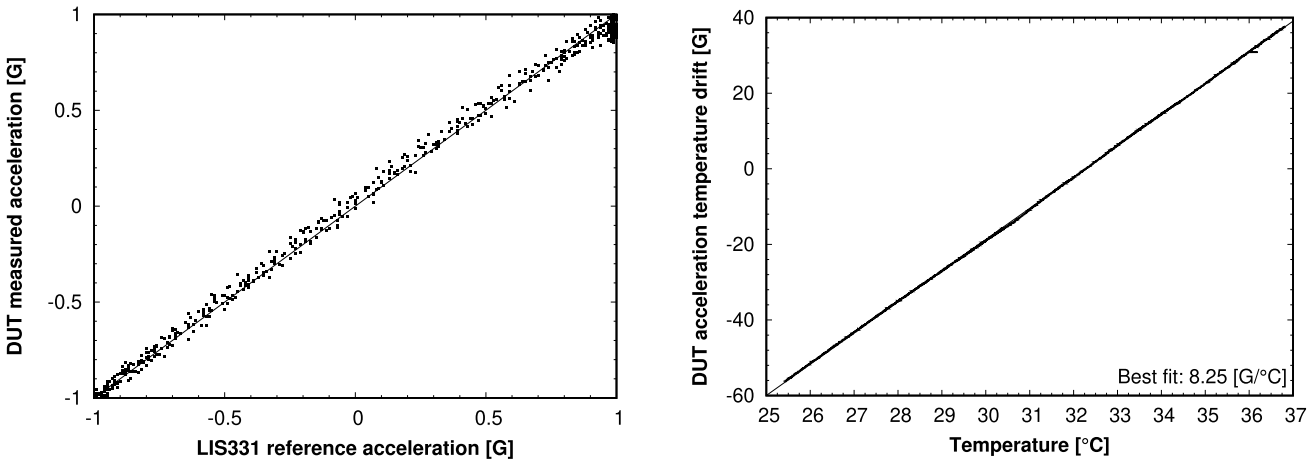

(a) (b)

Fig. 9. (a) *Z*-axis accelerometer linearity and (b) temperature behavior without compensation. For the linearity tests, a commercial LIS331 accelerometer was used as a reference for comparison.

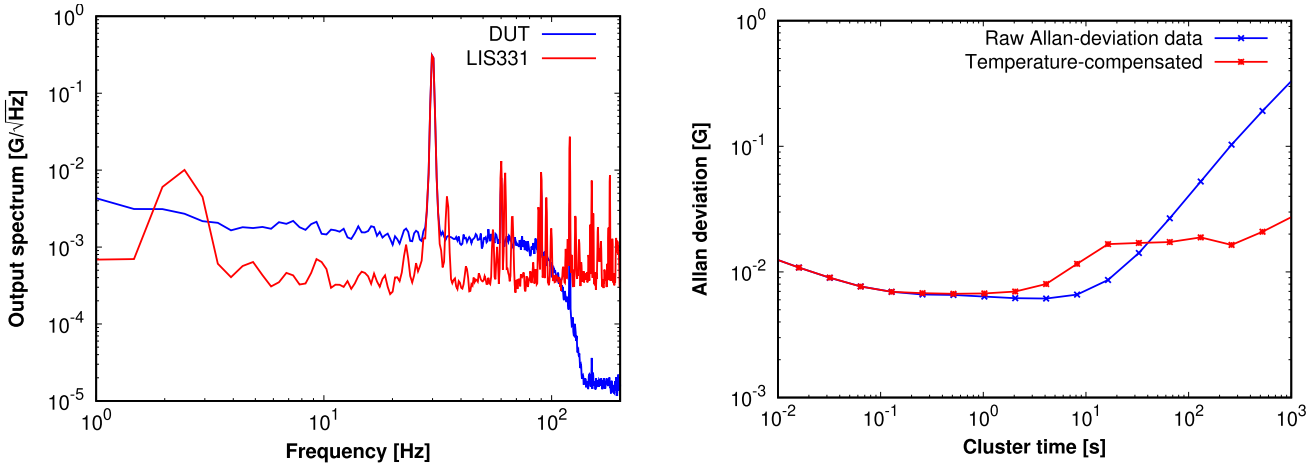

(a) (b)

Fig. 10. (a) Out-of-plane axis and reference accelerometers noise floor and output spectrum when driven by a 30-Hz signal. (b) Allan deviation over different cluster integration periods with and without temperature compensation.

by performing an Allan deviation analysis both before and after a first-order temperature compensation algorithm was implemented in the digital domain using an external temperature sensor [see Fig. 10(b)]. The results indicate that the accelerometer shows a good stability over time once the temperature effects are removed. The small error increase between 1- and 30-s cluster times in the temperature-compensated measurement, versus the noncompensated one, was attributed to transient temperature mismatch between the accelerometer and the temperature sensor. A monolithic integration of the temperature sensor should correct for this effect and provide a much flatter response.

2) In-Plane Axes: In Fig. 11(a), the linearity and the response with two different temperatures of the in-plane axes accelerometer are shown. As with its out-of-plane axis counterpart, the accelerometer shows excellent linearity. The temperature drift was also measured, reaching only 0.06 G/°C even before any temperature compensation due to its improved tolerance to out-of-plane plate deformation.

The accelerometer noise floor spectral density was also measured, as well as the output spectrum when applying a 20-Hz acceleration using a vibrating plate [see Fig. 11(b)]. The measured noise floor was 150 μG/(Hz)$^{1/2}$, being the limiting factor of the electronics noise due to its reduced sensitivity. As in the case of the out-of-plane axis, the experiments also show that our accelerometer generates far lesser frequency spurs than the commercial reference device.

IV. Pressure Sensor

Based on the numerous advantages of applicability, ability of integration, cost, and performance, the pressure sensor market in the recent years is rapidly growing with an important application niche in the wearable market. An absolute pressure sensor for atmospheric gases or barometer (i.e., a sensor that indicates what is the air pressure compared to vacuum) can provide information about the altitude or changes of altitude of the user or the device itself. As navigation is increasingly needed inside buildings (indoor navigation), where there is

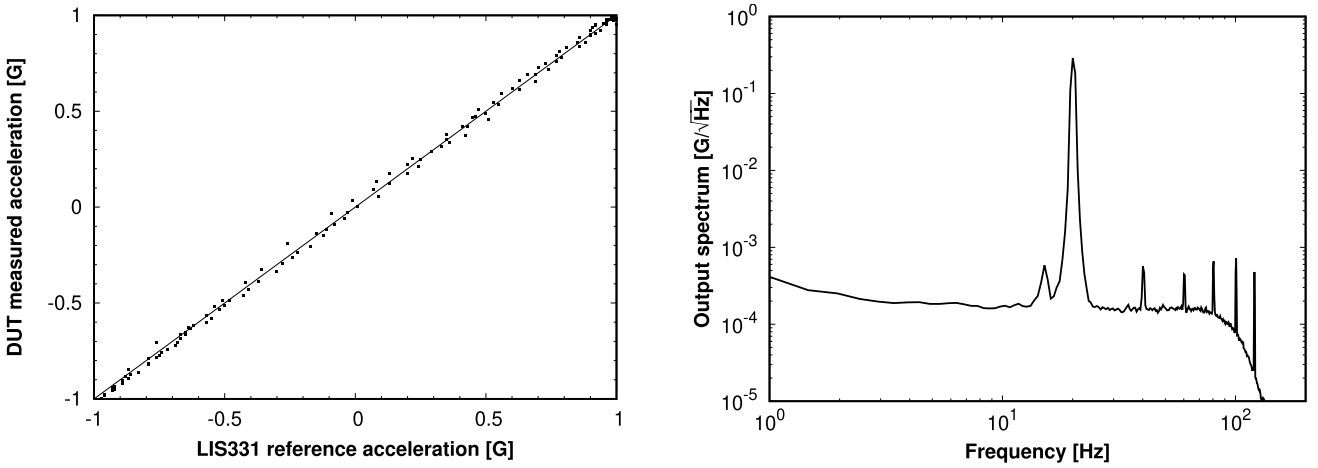

(a) (b)

Fig. 11. (a) In-plane axes accelerometer linearity and (b) noise floor and output spectrum when driven by a 20-Hz acceleration stimuli. A commercial LIS331 accelerometer was used as a reference for comparison.

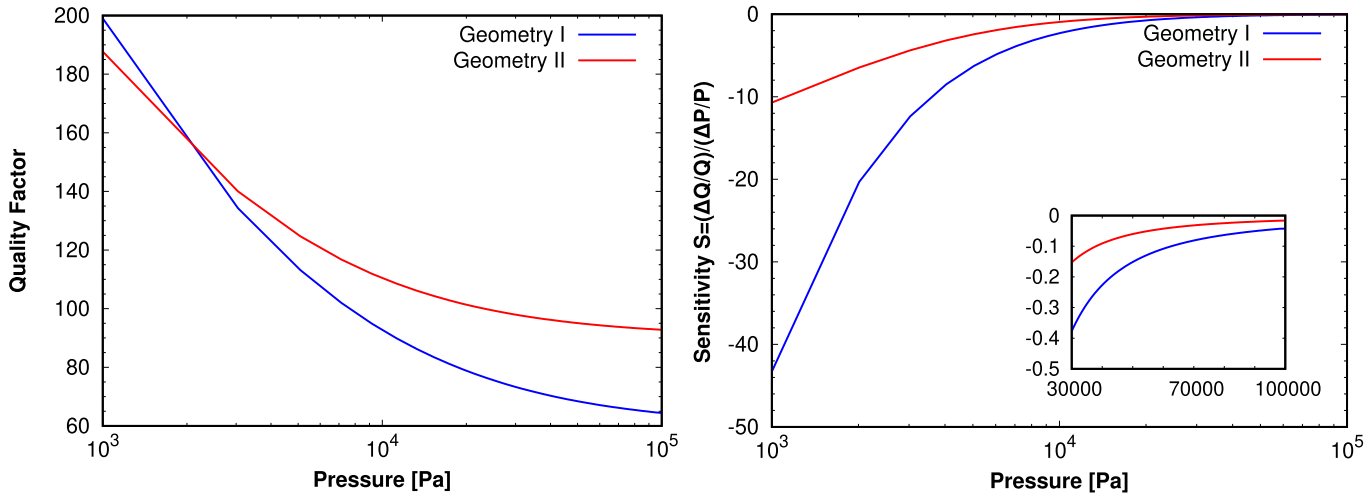

(a) (b)

Fig. 12. (a) Quality factor and (b) sensitivity versus pressure for two different geometries. Geometry I shows a higher sensitivity value and was thus selected for fabrication.

limited access to GPS signals, information about the pressure or altitude can be of great help to pinpoint the floor in which the device is [45]. Similarly, barometers can be used to assess depth in wells or caves during exploration, where battery duration is critical and no external reference signals are available. Many other applications will also arise from widespread adoption of a ubiquitous pressure sensor, for example, security enhancement of alarm systems as intrusion detectors in buildings [46], a worldwide-area network of pressure sensors for atmospheric data mining, and others [47].

There are several techniques [48] to build miniaturized absolute pressure sensors for atmospheric gases that can be suitable for wearable integration.

1) Pirani sensing, which relies on the thermal conductivity of gases [49]. By heating-up a filament and measuring its thermal loss, proportional to the molecules colliding with it, pressure can be estimated. Their main limitation is power consumption.
2) Membrane-deformation sensing, which relies on the deformation of a membrane that covers a vacuum-sealed cavity, caused by the air pressure difference between the external air pressure and the internal air pressure of the cavity. There are several variants of this sensor depending on how the membrane deformation is actually measured, the most important ones being capacitive [50] and piezoresistive [51] sensing.
3) Resonant-frequency sensing, based on the measurement of the resonant-frequency change at different pressures [52] of a microstructure due to the mechanical stress.
4) Quality-factor sensing, based on a resonator quality factor (Q) change with pressure [19], [20], [53].

Quality-factor sensing provides the most direct means of absolute pressure measurement without requiring a vacuum-sealed cavity (as membrane-deformation sensors do), without high power consumption (as Pirani-based devices) nor

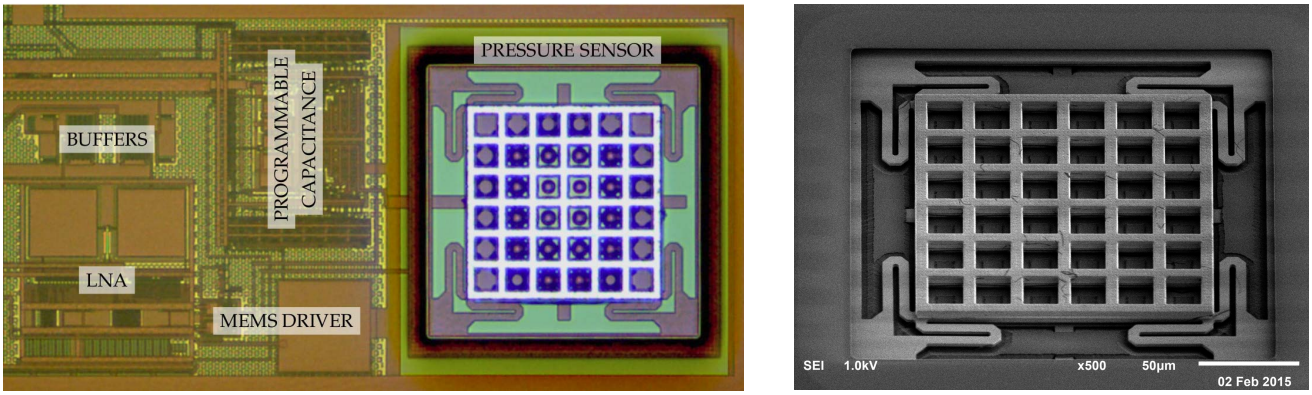

(a) (b)

Fig. 13. (a) ASIC optical microphotograph of the pressure sensor and its associated front-end electronics. (b) Pressure sensor SEM image after release.

indirect measurement techniques (as resonant-frequency sensing). They can be directly used in CMOS-MEMS-constrained scenarios, as they do not require the addition of new materials or complex manufacturing postprocesses. Combined with the other CMOS-MEMS sensors presented in this article, a compact, multisensor, low-power solution can be created that will avoid the drawbacks preventing a more widespread use of pressure sensors in wearable devices.

A. Operation Principle and Device Modeling

The resonator quality factor and the ambient pressure follow an approximate power relationship, primarily dependent on the surrounding fluid viscosity, i.e., air, in which the device is operated:

$$Q \approx a P^b \tag{5}$$

where a and b are coefficients relating the quality factor (Q) and the pressure (P), with b being a negative number (see [54, Sec. 4.3.3]). A realistic simulation of the quality factor dependence with the pressure for two different devices we studied is shown in Fig. 12(a). Frequently, instead of using the pressure, designers rely on a close-related parameter, the Knudsen number (Kn) (see [54, Sec. 4.3.2]) that measures the viscosity of the surrounding fluid; in other words, the degree of rarefaction of gases. The Knudsen number is a dimensionless quantity defined as the ratio of the gas molecular mean free path λ to the resonator gap z_0, i.e.,

$$Kn = \frac{\lambda}{z_0} = \frac{\lambda_0 P_0}{P z_0} \approx \frac{0.0068}{P z_0} \tag{6}$$

where P_0 and λ_0 are the ambient pressure and the mean free path at ambient pressure of the air molecules, respectively. For values of $Kn < 0.01$, air damping is essentially independent of the surrounding pressure. These cases are defined as being in the continuum-flow regime. For values of $0.01 < Kn < 0.1$, the device is said to operate in the slip-flow regime, and for $0.1 < Kn < 10$, with a mean free path comparable to the gap size, the device operates in the so-called transitional-flow regime. For $Kn < 10$ (free molecular-flow regime), the gas stops behaving like a viscous fluid and the individual molecules' interactions with the device become the main source of damping. For our device, having a 2.5-μm gap, the slip-flow regime is defined as 27 200 Pa $< P <$ 275 000 Pa, and this is 27.2 mbar $< P <$ 2.75 bar.

For allowing co-simulation of the sensor and the electronics, a realistic Verilog-A model of the sensor was developed [55]. It precisely mimics all the capacitive effects (including parasitics), the effect of pressure and temperature in the quality factor [56], [57], pull-in [58], voltage nonlinearities [59], Brownian noise [60], and manufacturing mismatch.

B. Device Design

As shown in Section IV-A, the Knudsen number allows a quick definition of the proper operating regimes in which the device must work at. Clearly, there will not be any Q sensitivity to pressure in the continuum flow, whereas it will start to be apparent in the slip flow. As the gap is a parameter that can only take a certain range of values limited by the CMOS manufacturing process and the device pull-in voltage, the only variable we can freely optimize is the damping value itself, so their variations are easily measurable by the electronics. An optimization process was done by setting a minimum device capacitance that the integrated electronics can sense on a fixed area, and sweeping the number, position, and size of the release holes in order to maximize the quality-factor variation with Kn [61]. For this, a device sensitivity (S) parameter was defined as the relative variation of the quality factor versus the relative variation of the pressure, i.e.,

$$S = \frac{\Delta Q/Q}{\Delta P/P} \tag{7}$$

thus allowing for direct performance comparison among two different geometries, namely, Geometries I and II, differing only on the number and size of holes [see Fig. 12(b)]. Finally, the optimized prototype had a square plate area of 140 × 140 μm and 6 × 6 perforations of 18 × 18 μm, leaving an air gap of 2.5 μm. Design details for each geometry are available in [61, Table I].

By using the Verilog-A pressure sensor model mentioned in Section IV-A, an application-specific integrated circuit (ASIC) containing the sensor and its front-end electronics was designed. Its microphotograph is shown in Fig. 13(a) and

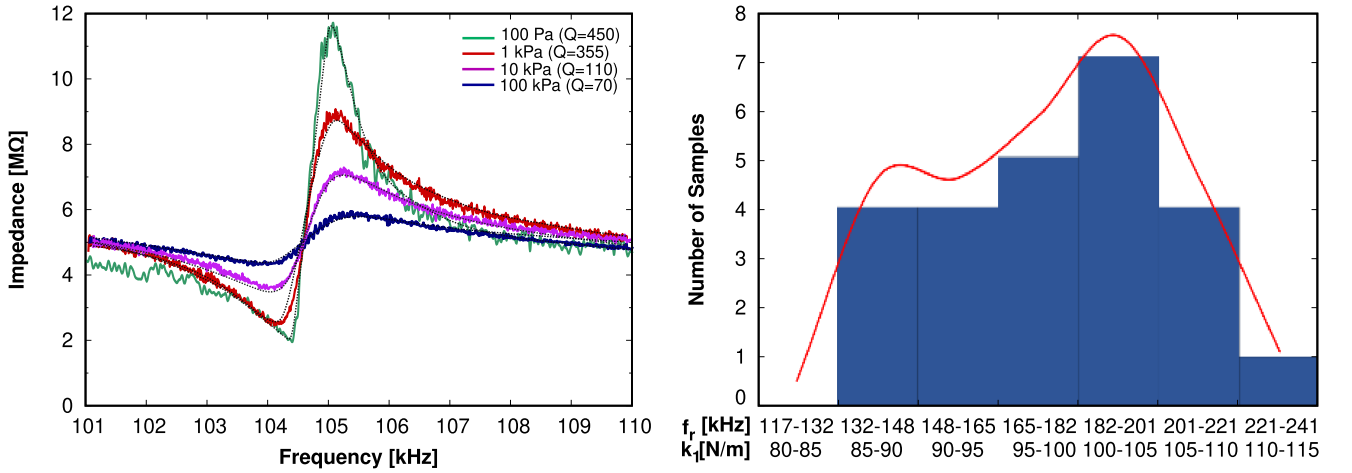

(a) (b)

Fig. 14. (a) Measured pressure sensor resonance peak (solid colored lines) compared with the simulation model (black dotted lines) for various ambient pressures from 100 Pa to 100 kPa. (b) Resonant-frequency mismatch histogram obtained from the measurements of 25 samples.

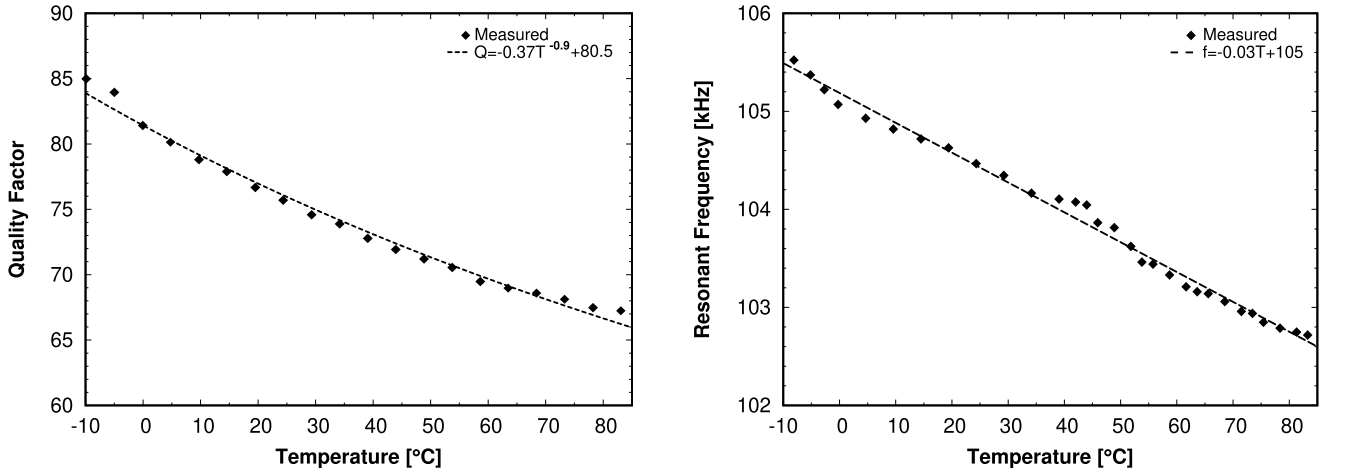

(a) (b)

Fig. 15. (a) Measured quality factor and (b) resonant-frequency dependence with temperature.

its SEM image in Fig. 13(b). The ASIC includes only the front-end electronics, that is, the one connected directly to the sensor. This research prototyping allows maintaining full performance while keeping the ASIC design investment effort low, as the remaining electronic blocks can be implemented outside, after the internal amplification of the ASIC has taken place. The integrated blocks are the low-noise amplifier (LNA) that amplifies the sensor capacitance variations, the buffers that allow connection with the external world, the programmable capacitance that mitigates the static offset capacitance of the sensor, and the MEMS driver that provides the voltage necessary for the sensor to correctly operate.

C. Measurements and Results

The measured pressure sensor resonance peak is shown in Fig. 14(a). Q changes from 70 at atmospheric pressure to 450 at 1 mbar, proving the operating principle of the device. The figure also shows the resonance peak as estimated by the Verilog-A model, showing an excellent alignment with the measured data.

For volume production, it is also necessary to demonstrate that the mismatch effects of batch manufacturing are under control. For our pressure sensor, mismatch has been estimated by measuring the resonant frequency of 25 different samples, as shown in Fig. 14(b). Another set of critical parameters to analyze is the dependencies with temperature. We have measured the Q-factor and the resonant-frequency variations with the temperature in Fig. 15(a) and (b), respectively, showing that a simple bandgap-based thermometer is enough to compensate for these variations [20].

V. Magnetic Sensor

There are several techniques to build a magnetic sensor depending on the range of the magnetic field required to be measured [62]. This range goes from 1 fT required for superconducting physics and quantum computing to 1 T required for machine positioning and rotation sensing using fixed magnets.

However, for the wearable integrated sensors, we are mainly interested in accurately measuring the Earth's magnetic field, so we know where the device is actually pointing to without needing any artificial reference (compass function). As the Earth's magnetic field intensity is in the range between 25 and 65 μT depending on the location [63], a sensor for accurately measuring the orientation with a few degrees of precision would require a sensitivity up to 300 nT while keeping a reasonable immunity to the locally generated magnetic fields (e.g., due to PCB currents) [15]. Among the sensing principles suitable for the integrated compass application, we can find the following.

1) Hall effect, in which a current flowing through a material in the presence of a magnetic field generates a measurable voltage perpendicular to both the current and the magnetic field. In order to reach sufficient sensitivity for this application, those sensors require magnetic concentrators to function [64], [65].
2) Flux gate, in which a driving coil periodically magnetizes a small core in one direction and then in the opposite direction, while a sensing coil measures the induced voltages during the magnetization reversal. The asymmetries detected are directly related to the external magnetic field [66]. Despite its costs in terms of power consumption and its need of a ferromagnetic core, a miniaturized version of this technology is currently manufactured commercially [67].
3) Anisotropic magnetoresistive, in which the electrical resistance of a material (usually a Permalloy derivative) depends on the angle and intensity between the electrical current and the direction of the magnetization [68]. They usually require magnetic concentrators to detect out-of-plane magnetic fields, but they can reach competitive costs and performance as commercial products [69].
4) Magnetic tunnel junction or tunnel magnetoresistors (TMRs), in which the resistance of the ferromagnetic layers varies depending on the external field intensity and direction [70]. There are also several products available commercially [71], as this type of sensor provides good accuracy and low power consumption.
5) Lorentz force, in which an alternating current flowing through a movable plate generates an alternating force on it proportional to the magnetic field strength. The plate displacement is then measured [15], [21], [72], [73], [74], usually with capacitance sensing. No commercial products are available as of this date.

When looking toward integration, it is clear that a CMOS-based, Lorentz-force magnetometer [15] can have important cost and size advantages, as the same manufacturing steps used for creating the proof-mass of the accelerometer and the pressure sensor can also be used for manufacturing the Lorentz resonator.

A. Operation Principle and Device Modeling

As stated before, the Lorentz-force MEMS magnetometer works by sensing the displacement of an MEMS resonator caused by the Lorentz force that appears when an external magnetic field is applied to a wire conducting a current. On a straight wire, this Lorentz force can be written as

$$\vec{F}_L = L\vec{I} \times \vec{B} \tag{8}$$

where L is the wire length, $\vec{I}$ is the magnitude and direction of the sensing current, and $\vec{B}$ is the magnetic field.

Usually, the Lorentz-force magnetometers use an alternating current at the resonant frequency of the MEMS resonator. This has two fundamental advantages: first, the sensed signal is already displaced in frequency—thus, the sensing electronics does not need a chopper modulator like the accelerometer to reduce the electronics flicker noise; and second, the resonance peak of the MEMS resonator amplifies the oscillation considerably. In this case, and considering only a single axis, the Lorentz force can be written as

$$F_L = \mathrm{ILBcos}\,(\omega t) \tag{9}$$

where ω is the angular frequency of the driving current. Applying this to the resonator model shown in Fig. 6 and using the second-order electromechanical model equation shown in (1), it yields

$$\mathrm{ILBcos}\,(\omega t) = m\frac{d^2z}{dt^2} + b\frac{dz}{dt} + kz. \tag{10}$$

By defining the angular resonant frequency as $\omega_0 = (\mathrm{k/m})^{1/2}$ and the quality factor as $Q = \omega_0$ m/b, we can solve (10) for the amplitude, thus yielding

$$|\,z\,| = \frac{\mathrm{ILB}/k}{\sqrt{\left(\dfrac{\omega^2}{\omega_0^2} - 1\right)^2 + \left(\dfrac{1}{Q}\dfrac{\omega}{\omega_0}\right)^2}} \tag{11}$$

which, considering that the driving current operates at the resonant frequency ($\omega = \omega_0$), simplifies to

$$|\,z\,| = Q\frac{\mathrm{ILB}}{k}. \tag{12}$$

Hence, applying the driving current at the resonant frequency of the structure increases the sensitivity by a factor of Q. As in the accelerometer case, capacitive readout is usually employed to detect the sensor movement, so the capacitance can be approximated by a parallel-plate capacitor model and then linearized using a Taylor approximation

$$C\,(B) \approx \frac{\varepsilon_0 A}{z_0 - z\,(B)} = \frac{\varepsilon_0 A}{z_0}\left(1 + B\frac{\mathrm{QIL}}{z_0 k}\right) + O\left(B^2\right). \tag{13}$$

B. Device Design

Two devices were manufactured for sensing the magnetic field: one sensitive to the out-of-plane field (vertical axis) and the other sensitive to the in-plane field (horizontal axis). By combining one out-of-plane sensor with two orthogonal in-plane, a full three-axis sensor was manufactured using the GlobalFoundries 0.18-μm ULL six-metal process. A dry release using vapors of hydrogen fluoride (vHFs) was performed, and then, residues were removed by a 1-min bake at 250 °C in air. Unlike the standard liquid HF acid release, the

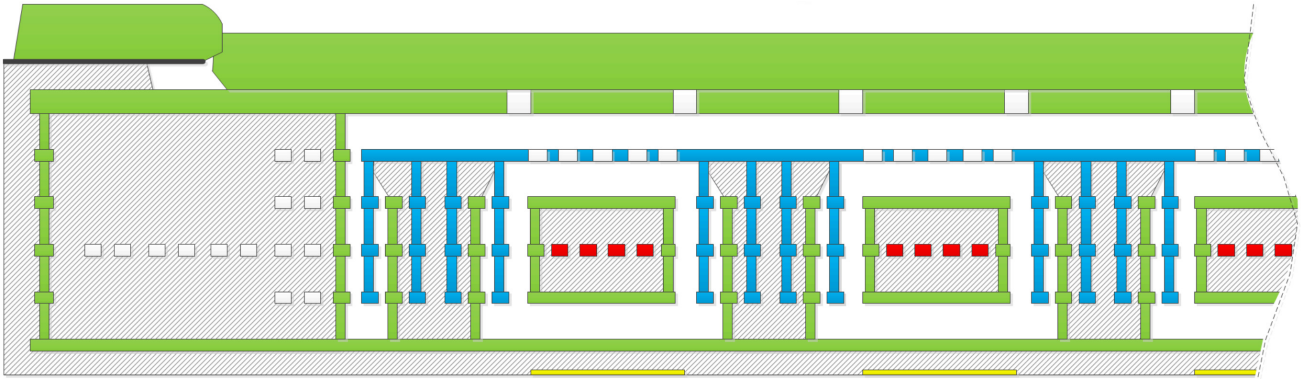

Fig. 16. Magnetometer MEMS sensor structure for the in-plane magnetic fields. The shield plate is shown in green, the sense plate is shown in blue, the wire is shown in red, and the calibration coil is shown in yellow. Three sensing beams are shown in the picture, surrounding the wires. Dashed lines indicate the silicon oxide (SiO_2) dielectric.

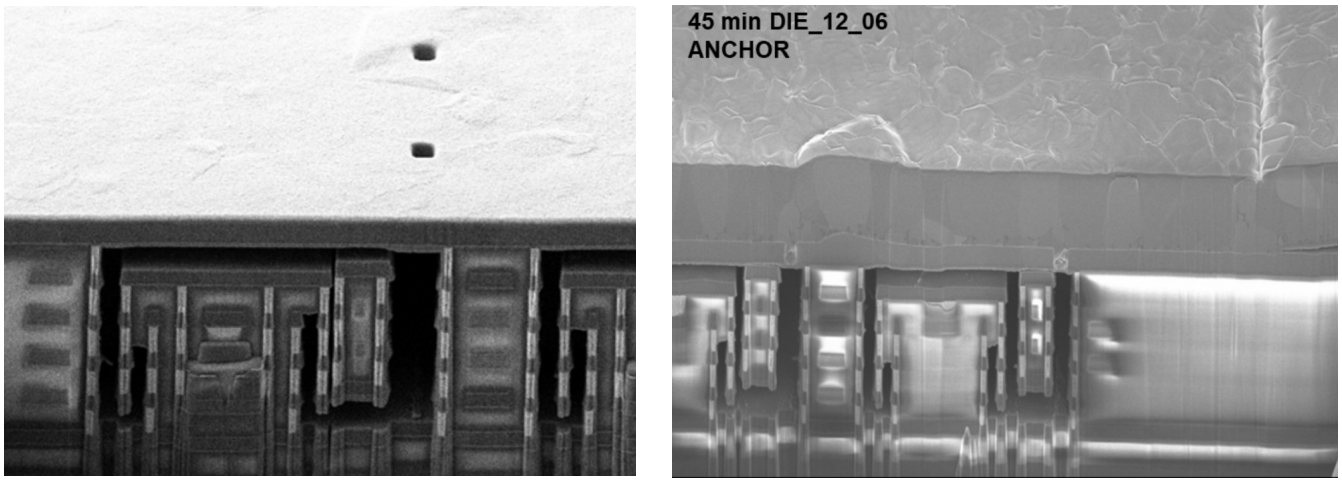

(a) (b)

Fig. 17. SEM images taken over FIB cuts of the manufactured out-of-plane axis magnetic sensor (a) after release but before sealing and (b) after release and sealing. The in-plane sensor SEM images can be seen in Fig. 4.

vHF can cause damage to the passivation layer [75]; however, this inconvenience was easily overcome by increasing the silicon content of the Si_3N_4 passivation layer, as reported in [76]. The devices were sealed in vacuum using aluminum sputtering deposition and then packaged in a standard low-cost plastic-molded QFN 16-pin 4 × 4 mm. The pressure inside the cavity was estimated to be below 200 μbar after sealing and packaging and about 2.5 mbar after an HTS JESD22-A103D test (consisting of 1100-h storage at 150 °C) was performed.

The Lorentz-force MEMS magnetometer sensor has four key structural parts necessary for its proper operation.

1) Sense plate, which is connected to the LNA and forms the fixed plate of the sensing capacitance.
2) Shield plate, which connects to a plate surrounding the Lorentz current wire and prevents capacitive feed-through between the Lorentz wires and the sensing plate. Together with the sense plate, it defines the sensing capacitance. An ac voltage may be applied between this plate and the sensing plate to keep the sensor oscillating at the resonant frequency if the magnetic field is too small [77].
3) Lorentz wire, which carry the Lorentz current. Together with the shield plate, they form the movable plate of the sensor. For practical reasons, the wire is split in a series of beams mechanically coupled together.
4) Calibration coil, which connects to a miniaturized coil that allows generating a localized magnetic field for calibrating the sensor sensitivity.

Fig. 16 shows the sensor structure for the in-plane (XY) magnetic fields. A magnetic field on the horizontal direction will generate a vertical displacement on the movable plate that can be sensed as a capacitance change between the sense and the shield plates. Note that each wire crosses multiple times each electrode, thus allowing for an enhanced sensitivity. SEM images of this sensor before and after the sealing can be seen in Fig. 4. The sensor structure for detecting the out-of-plane magnetic field (Z) is very similar, but it senses the lateral movement by taking advantage of an asymmetrical disposition of the sense and shield plates, as shown in [15]. Its SEM images before and after the sealing can be seen in Fig. 17.

C. Measurements and Results

The sensor electronics was implemented using discrete components on a PCB. Albeit not providing the best figures in terms of performance, this approach gives the greatest flexibility in the early design stages of the system. The architecture

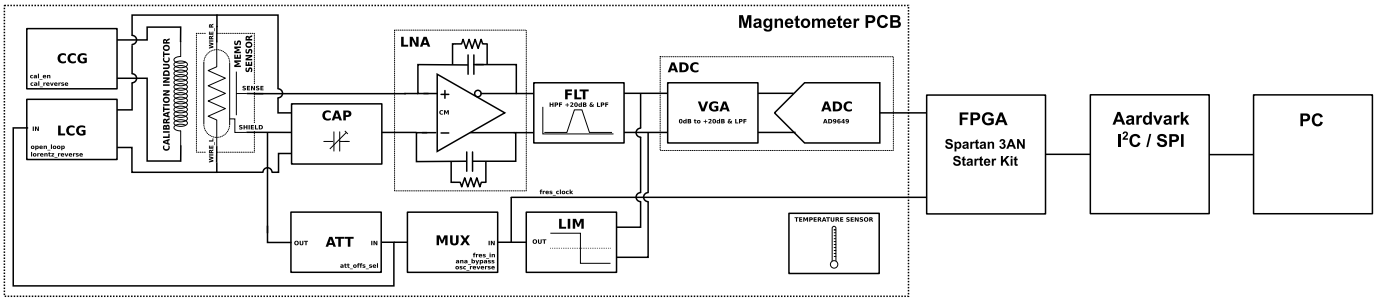

Fig. 18. Architecture and design partitioning of the magnetometer sensing electronics. The magnetometer PCB includes all the sensor front end and the reference thermometer for temperature corrections, and the FPGA board performs the demodulation of the signal and the closed-loop control, the Aardvark functions as I^2C to USB bridge, and the PC serves as data-logger.

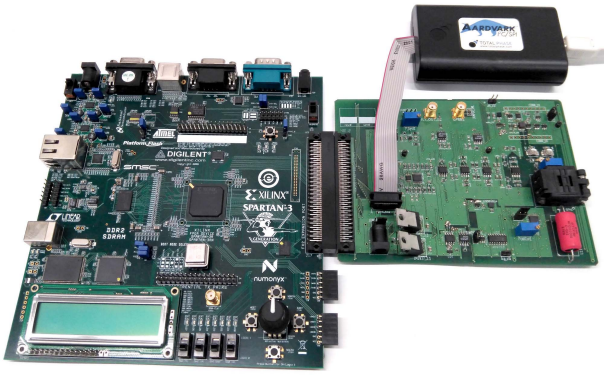

Fig. 19. Magnetometer prototype setup. Left: Xilinx Spartan 3AN FPGA board. Right: magnetometer PCB and the Aardvark communication bridge. The sensor is placed in the socket of the right of the magnetometer PCB.

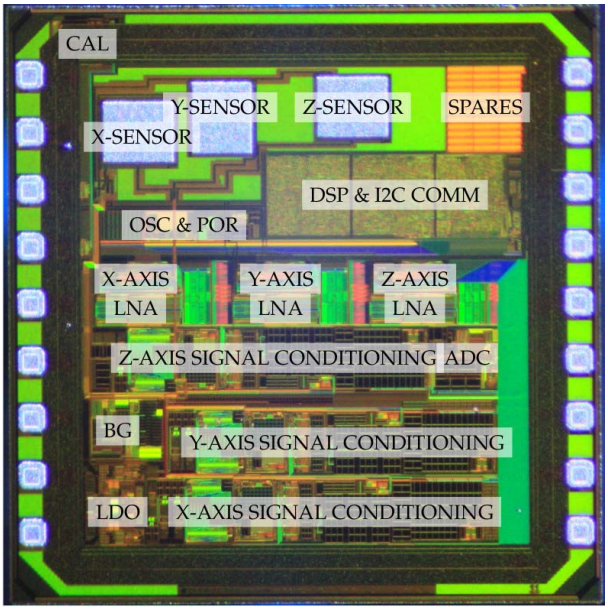

Fig. 20. ASIC containing magnetic sensors for *X*-, *Y*-, and Z-axes along all postprocessing electronics.

is based on a closed-loop approach [77], as shown in Fig. 18. The closed-loop approach allows tracking the sensor resonant frequency by using a limiter for detecting when the sensor oscillation sign changes, thus changing to the ac Lorentz current sign and the electrostatic driving polarity, effectively creating a self-sustained oscillation loop. The photograph of the whole system is shown in Fig. 19. Besides the PCB, a fully monolithic experimental ASIC was successfully manufactured (see Fig. 20). It contains all three sensors, one per axis, with their associated LNA and signal-conditioning chains, as well as a bandgap (BG) reference circuit, a low-dropout (LDO) voltage regulator, a calibration-current generator for the sensors (CAL), an analog-to-digital converter (ADC), a digital signal processor (DSP), and an I^2C communication engine.

The magnetometer noise and heading accuracy versus the cavity pressure is shown in Fig. 21. Cavity pressure is a critical manufacturing figure, as it directly impacts the quality factor of the mechanical resonator and, hence, the magnetometer sensitivity, as shown by (12). Due to the complexity of the sensitivity experiments, a characterization platform was designed to simplify the test setup and ease the test operations of wafer-level unpackaged devices [78].

Different beam lengths ranging from 100 to 800 μm were tested with a square-wave Lorentz current of 0.6 mA. As the total wire length increases with the beam length, the total wire resistance also increases and, thus, the dissipated power by the sensor. The measured cavity-pressure range after standard plastic-molded QFN packaging and the rapid-aging HTS test is also shown, indicating an rms heading accuracy better than $0.2°/(\text{Hz})^{1/2}$ for the 200 μm device.

The effect of temperature on the quality factor (Q) is shown in Fig. 22(a) for the open-cavity case (pressure is kept constant at 4 mbar, thus revealing only the changes due to the device itself) and in Fig. 22(b) for the closed-cavity case (pressure is free to change due to the temperature). Note that the sensors by themselves only show small variations with temperature, but when they are enclosed, the effect of the closed cavity is noticeable. As sensitivity is a key figure, Q must be maximized, so the device must be enclosed in a cavity that maintains vacuum. The MEMS cavity itself can be used for that, as long as the release holes are sealed afterward, as shown in Figs. 4 and 17(b).

Shock tests between 3000 and 6000 G were performed in all three axes, resulting in no measurable performance effects. Measured yield after packaging in a low-cost plastic mold in

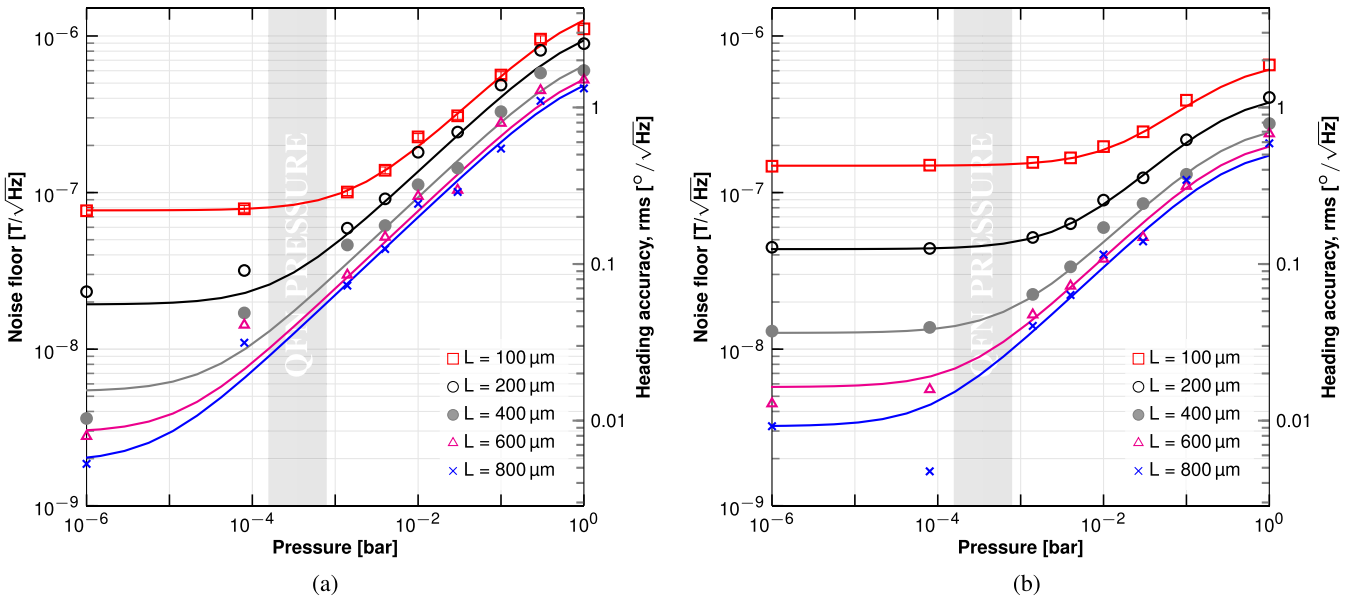

Fig. 21. MEMS Brownian noise floor and heading accuracy versus cavity pressure for different beam lengths for out-of-plane and in-plane sensing devices. The Lorentz current was set to 0.6 mA (square wave). The number of beams and wires is kept constant. Heading accuracy or angle error is calculated assuming $B_{earth} = 20$ μT. (a) Z device (out-of-plane) with $g = 0.35$ μm. (b) XY device (in plane) with $g = 0.9$. μm.

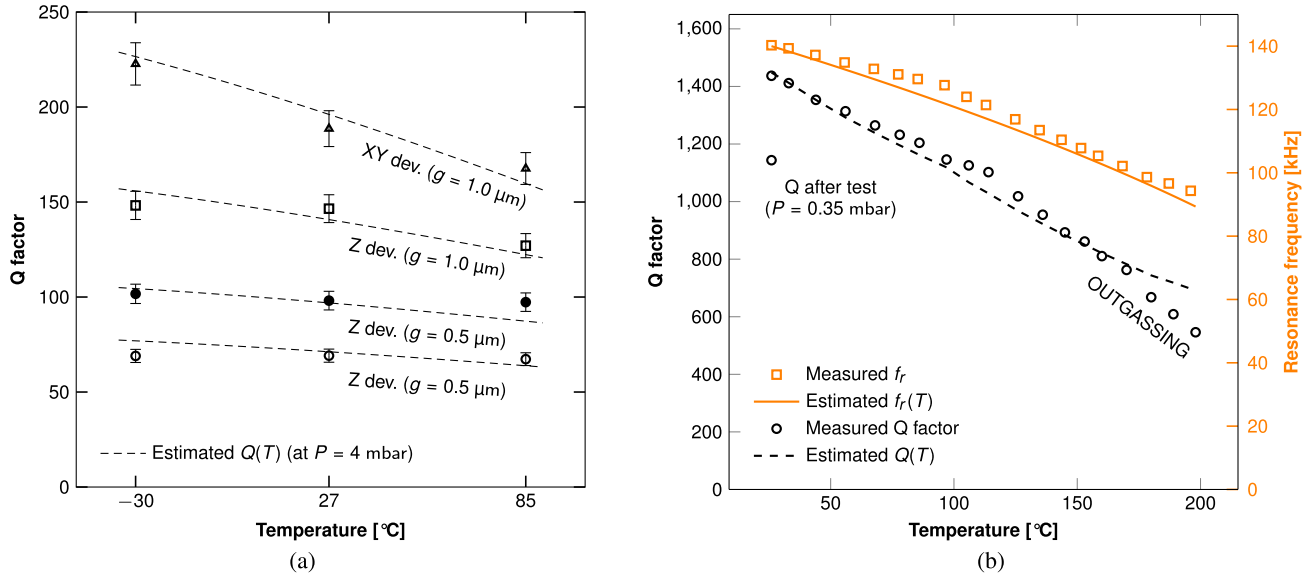

Fig. 22. Measured and predicted values of f_r and Q-factor as a function of temperature. (a) Open-cavity quality factor (Q) versus temperature measured on wafer at constant $P = 4$ mbar. (b) Z-axis open-cavity quality factor (Q) and resonant frequency f_r versus temperature, measured on closed cavity before the HTS tests. The estimated cavity pressure is $P = 0.28$.

QFN reached 95% for some variants, while temperature-stress tests showed none or little yield loss after a postprocessing at 450 °C for 30 min followed by 400 °C for 1 h, thus proving the potential of the technology for mass production (see [15]). A performance comparison table with other commercial and research devices can also be seen in [15, Table IX].

VI. Future of CMOS-MEMS

The design of MEMS sensors and actuators using the CMOS manufacturing line is very process-dependent [8]. Special design techniques must be used to overcome the inherent CMOS process limitations and uncontrolled mechanical characteristics [16]. As the CMOS processes and packaging techniques are always evolving, some considerations must be made on how these will impact the CMOS-MEMS monolithic manufacturing.

CMOS evolution is not just due to lithography resolution improvements, the process itself also changes significantly. For example, nodes below 130 nm use copper instead of aluminum for the metallization. Besides the significant difference in density, Young modulus, and other mechanical parameters of copper versus aluminum, its use as a structural material will notably affect the release, as the selectivity of vHF etching to copper is notably worse [79]. Moreover, the damascene

manufacturing technique typically used in CMOS copper deposition has capping layers of silicon nitride on each metal level [80], blocking the oxide etching below it in the same way that the silicon nitride passivation allows us to protect the electronics part from being damaged during the MEMS release [81]. Hence, it seems likely that a new set of release techniques and tools will have to be developed for advanced nodes.

Technology evolution itself is not the only threat to the CMOS-MEMS future. Cost, one of the significant advantages of CMOS-MEMS monolithic co-fabrication, can also become a drawback. Silicon real-state cost significantly increases as the features shrink. For example, the current full-wafer cost in a 90-nm process is estimated to be $1650, while for 5 nm, it is expected to be ten times higher [82]. In a purely digital design, this increased wafer cost is vastly compensated by a much higher gate density, resulting in much smaller chips for the same gate count. Overall, for a purely digital chip, this reduces the cost-per-chip by a factor of 10 between the same process nodes despite the wafer price increase [82]. MEMS, however, cannot be scaled in the same way as digital CMOS. For example, some key mechanical specifications, most notably the mass in the case of an accelerometer, cannot be arbitrarily reduced without sacrificing performance. The same applies to analog or RF CMOS design, where it is becoming common to use chiplets [83] to combine several chips manufactured with different processes in a single package. Chiplets may eventually offset the cost advantages of CMOS-MEMS monolithic integration, in addition to decoupling the higher electronics manufacturing yield from the lower MEMS one.

However, other key advantages of the CMOS-MEMS monolithic integration approach seem more likely to remain in place. For example, the additional performance gain due to the lower parasitics involved, as no interconnection pads are needed between the MEMS and its associated signal-conditioning electronics, or the cost advantage in less-complex products not requiring per se high-cost manufacturing processes or advanced packaging technologies.

VII. Conclusion

A manufacturing flow to develop CMOS-MEMS sensors has been designed over the last years, including their operation principle, device design, modeling, and measurements of some key sensors. The post-CMOS class processing flow is performed after full standard CMOS processing, and it can be carried out with simple processing steps, compatible with the CMOS fabricated devices. The technique is based on the wet- or vapor-etch release of BEOL materials, specifically aluminum layers as MEMS structures and silicon oxide as the sacrificial material. The etched regions are confined by means of isolation using reported configurations of passivation, vias, and metals. The MEMS typically uses a set of metals, but the lower unused metals and front end of line (FEOL) can be equally utilized, when possible, to embed active devices below the MEMS if area occupancy has to be optimized.

As proof examples, the full designs of triaxial accelerometers, pressure sensors, and triaxial magnetometers have been reported and explained in detail. Accelerometers are based on the vertical or lateral inertial movement of a proof mass and capacitive detection. Pressure sensors are based on the detection of the quality factor (Q) variation of a resonant membrane as a function of air pressure that produces changes in viscosity. The magnetometers capacitively detect the amplitude variation of a resonant system changed by the Lorentz force produced by the magnetic field in conjunction with a current. Original decoupling structures allow to minimize interference between the Lorentz force and the electrostatic signal in the measurement. In order to co-simulate the micromechanical devices together with the electronics conditioning circuits, the MEMS has been characterized and Verilog-A models have been developed.

The sensors have been manufactured on different ASICs, including conditioning electronics for each case. Experimental results that confirm good or even excellent performance when compared to current commercial devices have been presented. The reported accelerometers show good linearity when compensated in temperature and a noise floor of 150 $\mu\text{G}/(\text{Hz})^{1/2}$ for the out-of-plane axis and 1.5 $\text{mG}/(\text{Hz})^{1/2}$ for in-plane axes. Allan deviations also show good stability. The pressure sensor shows a Q sensitivity of -0.04 at atmospheric pressure, increasing as the pressure is reduced, while the magnetometer shows rms heading accuracy better than $0.2°/(\text{Hz})^{1/2}$, and a sensitivity that can be adjusted by the amount of current, with no hysteresis effects as no magnetic materials are used.

In summary, it has been demonstrated that the CMOS technology can be used to integrate MEMS on a single die so that multisensor chips integrating signal conditioning and high-level digital postprocessing on the same die are feasible.

Acknowledgment

The authors would like to thank the reviewers for their valuable comments and suggestions, which were fundamental in improving the manuscript's quality.

References

[1] R. Tummala and M. Swaminathan, *Introduction to System-on-Package (SOP): Miniaturization of the Entire System*. New York, NY, USA: McGraw-Hill, 2008.

[2] O. Brand, "Microsensor integration into systems-on-chip," *Proc. IEEE*, vol. 94, no. 6, pp. 1160–1176, Jun. 2006. [Online]. Available: http://ieeexplore.ieee.org/iel5/5/34642/01652903.pdf?tp=&isnumber=&arnumber=1652903

[3] D. L. Hall and J. Llinas, "An introduction to multisensor data fusion," *Proc. IEEE*, vol. 85, no. 1, pp. 6–23, Jan. 1997.

[4] *Invensense MPU-9250 Nine-Axis (Gyro + Accelerometer + Compass) Datasheet*, TDK InvenSense, San Jose, CA, USA, 2015.

[5] *ST Microelectron. LSM9DS1 Nine-Axis (Gyro + Accelerometer + Compass) Datasheet*, Stmicroelectron., Geneva, Switzerland, 2015.

[6] *Bosch Sensortec BMX160 Nine-Axis (Gyro + Accelerometer + Compass) Datasheet*, Bosch Sensortec, Reutlingen, Germany, 2020.

[7] H. Qu, "CMOS MEMS fabrication technologies and devices," *Micromachines*, vol. 7, p. 14, Jan. 2016, doi: 10.3390/mi7010014.

[8] J. Valle, D. Fernandez, O. Gibrat, and J. Madrenas, "Manufacturing issues of BEOL CMOS-MEMS devices," *IEEE Access*, vol. 9, pp. 83149–83162, 2021. [Online]. Available: https://ieeexplore.ieee.org/document/9447709

[9] H. Baltes, O. Brand, A. Hierlemann, D. Lange, and C. Hagleitner, "CMOS MEMS—Present and future," in *Proc. IEEE Int. Conf. 15th IEEE Int. Conf. Micro Electro Mech. Syst.*, Jan. 2002, pp. 459–466. [Online]. Available: http://ieeexplore.ieee.org/iel5/7726/21214/00984302.pdf?tp=&isnumber= &arnumber=984302

[10] D. Fernández, "Arquitecturas y circuitos CMOS para el control, generación y procesado de señal de MEMS," Ph.D. dissertation, Universitat Politècnica de Catalunya, Barcelona, Spain, 2008. [Online]. Available: http://www.tdx.cat/TDX-0312109-130622

[11] D. Fernández, J. Ricart, and J. Madrenas, "Experiments on the release of CMOS-micromachined metal layers," *J. Sensors*, vol. 2010, pp. 1–7, 2010, doi: 10.1155/2010/937301.

[12] A. C. Fischer et al., "Integrating MEMS and ICs," *Microsyst. Nanoeng.*, vol. 1, p. 15005, May 2015, doi: 10.1038/micronano.2015.5.

[13] P. Michalik, D. Fernández, M. Wietstruck, M. Kaynak, and J. Madrenas, "Experiments on MEMS integration in 0.25 μm CMOS process," *Sensors*, vol. 18, no. 7, p. 2111, Jun. 2018, doi: 10.3390/s18072111.

[14] H.-Y. Chen, S.-S. Li, and M.-H. Li, "A low impedance CMOS-MEMS capacitive resonator based on metal-insulator-metal (MIM) capacitor structure," *IEEE Electron Device Lett.*, vol. 42, no. 7, pp. 1045–1048, Jul. 2021, doi: 10.1109/LED.2021.3081365.

[15] J. J. Valle, J. M. Sánchez-Chiva, D. Fernández, and J. Madrenas, "Design, fabrication, characterization and reliability study of CMOS-MEMS lorentz-force magnetometers," *Microsyst. Nanoeng.*, vol. 8, no. 1, p. 103, Sep. 2022, doi: 10.1038/s41378-022-00423-w.

[16] J. Valle, D. Fernández, J. Madrenas, and L. Barrachina, "Curvature of BEOL cantilevers in CMOS-MEMS processes," *J. Microelectromech. Syst.*, vol. 26, no. 4, pp. 895–909, Aug. 2017, [Online]. Available: http://ieeexplore.ieee.org/document/7924353/

[17] P. Michalik, J. M. Sánchez-Chiva, D. Fernández, and J. Madrenas "CMOS BEOL-embedded lateral accelerometer," in *Proc. IEEE Sensors*, Nov. 2015, pp. 1–4, doi: 10.1109/ICSENS.2015.7370516.

[18] P. Michalik, J.-M. Sánchez-Chiva, D. Fernández, and J. Madrenas, "CMOS BEOL-embedded z-axis accelerometer," *Electron. Lett.*, vol. 51, no. 11, pp. 865–867, 2015, doi: 10.1049/el.2015.0140.

[19] S. Banerji, J. Madrenas, and D. Fernandez, "Optimization of parameters for CMOS MEMS resonant pressure sensors," in *Proc. Symp. Design, Test, Integr. Packag. MEMS/MOEMS (DTIP)*, Apr. 2015, pp. 1–6. [Online]. Available: http://ieeexplore.ieee.org/stamp/stamp.jsp?tp=&arnumber=7160984

[20] S. Banerji, D. Fernández, and J. Madrenas, "Characterization of CMOS-MEMS resonant pressure sensors," *IEEE Sensors J.*, vol. 17, no. 20, pp. 6653–6661, Oct. 2017, [Online]. Available: http://ieeexplore.ieee.org/document/8022865/

[21] J. M. Sánchez-Chiva, J. Valle, D. Fernández, and J. Madrenas, "A CMOS-MEMS BEOL 2-axis Lorentz-force magnetometer with device-level offset cancellation," *Sensors*, vol. 20, no. 20, pp. 1–20, 2020. [Online]. Available: https://www.mdpi.com/1424-8220/20/20/5899

[22] M. Kaynak et al., "BEOL embedded RF-MEMS switch for mm-wave applications," in *IEDM Tech. Dig.*, Dec. 2009, pp. 1–4, doi: 10.1109/IEDM.2009.5424219.

[23] M. Kaynak et al., "Characterization of an embedded RF-MEMS switch," in *Proc. Top. Meeting Silicon Monolithic Integr. Circuits RF Syst. (SiRF)*, Jan. 2010, pp. 144–147, doi: 10.1109/SMIC.2010.5422816.

[24] J. L. Lopez et al., "Mixing in a 220 MHz CMOS-MEMS," in *Proc. IEEE Int. Symp. Circuits Syst.*, May 2007, pp. 2630–2633, doi: 10.1109/ISCAS.2007.377953.

[25] J. L. Lopez et al., "Double-ended tuning fork resonator in 0.35 um CMOS technology for RF applications," in *Proc. Ph.D. Res. Microelectron. Electron.*, 2008, pp. 89–92, doi: 10.1109/RME.2008.4595732.

[26] J. Verd et al., "Monolithic mass sensor fabricated using a conventional technology with attogram resolution in air conditions," *Appl. Phys. Lett.*, vol. 91, no. 1, Jul. 2007, Art. no. 013501. [Online]. Available: http://link.aip.org/link/?APL/91/013501/1501/1

[27] W.-C. Chen, W. Fang, and S.-S. Li, "A generalized CMOS-MEMS platform for micromechanical resonators monolithically integrated with circuits," *J. Micromech. Microeng.*, vol. 21, no. 6, May 2011, Art. no. 065012, doi: 10.1088/0960-1317/21/6/065012.

[28] Y. Guo, H. Ma, J. Lan, Y. Liao, and X. Ji, "Impact of various thermistors on the properties of resistive microbolometers fabricated by CMOS process," *Micromachines*, vol. 13, no. 11, p. 1869, Oct. 2022, doi: 10.3390/mi13111869.

[29] S. S. Bedair and G. K. Fedder, "CMOS MEMS oscillator for gas chemical detection," in *Proc. IEEE Sensors*, vol. 2, Oct. 2004, pp. 955–958.

[30] S. Gorreta et al., "Pulsed digital oscillators for electrostatic MEMS," *IEEE Trans. Circuits Syst. I, Reg. Papers*, vol. 59, no. 12, pp. 2835–2845, Dec. 2012. [Online]. Available: http://ieeexplore.ieee.org/stamp/stamp.jsp?tp=&arnumber=6248713

[31] *SilTerra Technology Overview*. Accessed: Dec. 7, 2022. [Online]. Available: https://www.silterra.com/technology/technology

[32] E. Ledesma, I. Zamora, J. Yanez, A. Uranga, and N. Barniol, "Single-cell system using monolithic PMUTs-on-CMOS to monitor fluid hydrodynamic properties," *Microsyst. Nanoeng.*, vol. 8, no. 1, p. 76, Jul. 2022, doi: 10.1038/s41378-022-00413-y.

[33] I. Zamora, E. Ledesma, A. Uranga, and N. Barniol, "High accuracy ultrasound micro-distance measurements with PMUTs under liquid operation," *Sensors*, vol. 21, no. 13, p. 4524, Jul. 2021.

[34] I. Zamora, E. Ledesma, A. Uranga, and N. Barniol, "Monolithic single PMUT-on-CMOS ultrasound system with +17 dB SNR for imaging applications," *IEEE Access*, vol. 8, pp. 142785–142794, 2020.

[35] J. Valle, D. Fernández, and J. Madrenas, "Experimental analysis of vapor HF etch rate and its wafer level uniformity on a CMOS-MEMS process," *J. Microelectromech. Syst.*, vol. 25, no. 2, pp. 401–412, Apr. 2016, doi: 10.1109/JMEMS.2016.2533267.

[36] F. M. D'Heurle, "Aluminum films deposited by RF sputtering," *Metall. Mater. Trans. B*, vol. 1, no. 3, pp. 725–732, Mar. 1970, doi: 10.1007/BF02811600.

[37] L. M. Roylance and J. B. Angell, "A batch-fabricated silicon accelerometer," *IEEE Trans. Electron Devices*, vol. ED-26, no. 12, pp. 1911–1917, Dec. 1979.

[38] D. W. Burns, R. D. Horning, W. R. Herb, J. D. Zook, and H. Guckel, "Sealed-cavity resonant microbeam accelerometer," *Sens. Actuators A, Phys.*, vol. 53, nos. 1–3, pp. 249–255, 1996. [Online]. Available: http://www.sciencedirect.com/science/article/pii/0924424796011351

[39] T. A. Roessig, R. T. Howe, A. P. Pisano, and J. H. Smith, "Surface-micromachined resonant accelerometer," in *Proc. Int. Conf. Solid State Sens. Actuators (Transducers)*, Chicago, IL, USA, vol. 2, Jun. 1997, pp. 859–862.

[40] H. K. Rockstad, T. W. Kenny, J. K. Reynolds, W. J. Kaiser, and T. B. Gabrielson, "A miniature high-sensitivity broad-band accelerometer based on electron tunneling transducers," *Sens. Actuators A, Phys.*, vol. 43, nos. 1–3, pp. 107–114, May 1994. [Online]. Available: http://www.sciencedirect.com/science/article/pii/092442479300676U

[41] F. Mailly, A. Giani, A. Martinez, R. Bonnot, P. Temple-Boyer, and A. Boyer, "Micromachined thermal accelerometer," *Sens. Actuators A, Phys.*, vol. 103, no. 3, pp. 359–363, Feb. 2003. [Online]. Available: http://www.sciencedirect.com/science/article/pii/S0924424702004284

[42] F. Rudolf, "A micromechanical capacitive accelerometer with a two-point inertial-mass suspension," *Sens. Actuators*, vol. 4, pp. 191–198, Jan. 1983. [Online]. Available: http://www.sciencedirect.com/science/article/pii/0250687483850240

[43] M.-H. Tsai, C.-M. Sun, W.-J. Mao, and W. Fang, "The CMOS-MEMS 3-axis capacitive accelerometer to meet the commercial specifications," in *Proc. IEEE 29th Int. Conf. Micro Electro Mech. Syst. (MEMS)*, Jan. 2016, pp. 1002–1005.

[44] J. M. Sanchez-Chiva, P. Michalik, D. Fernandez, and J. Madrenas, "A CMOS BEOL accelerometer low-noise readout amplifier with 4.2 zF/$\sqrt{\text{Hz}}$ total noise floor," in *Proc. IEEE SENSORS*, Nov. 2015, pp. 1–4, doi: 10.1109/ICSENS.2015.7370635.

[45] G. Liu et al., "Beyond horizontal location context: Measuring elevation using smartphone's barometer," in *Proc. ACM Int. Joint Conf. Pervasive Ubiquitous Comput., Adjunct Publication*, New York, NY, USA, Sep. 2014, p. 459, doi: 10.1145/2638728.2641670.

[46] M. Wu, P. H. Pathak, and P. Mohapatra, "Monitoring building door events using barometer sensor in smartphones," in *Proc. ACM Int. Joint Conf. Pervasive Ubiquitous Comput. (UbiComp)*, New York, NY, USA, 2015, p. 319, doi: 10.1145/2750858.2804257.

[47] X. Su, H. Tong, and P. Ji, "Activity recognition with smartphone sensors," *Tsinghua Sci. Technol.*, vol. 19, no. 3, pp. 235–249, Jun. 2014.

[48] M. Elwenspoek, R. Wiegerink, and R. J. Wiegerink, *Mechanical Microsensors*. Berlin, Germany: Springer, 2001.

[49] A. M. Robinson, P. Haswell, R. P. W. Lawson, and M. Parameswaran, "A thermal conductivity microstructural pressure sensor fabricated in standard complementary metal-oxide semiconductor," *Rev. Sci. Instrum.*, vol. 63, no. 3, pp. 2026–2029, Mar. 1992, doi: 10.1063/1.1143160.

[50] K. Kasten, J. Amelung, and W. Mokwa, "CMOS-compatible capacitive high temperature pressure sensors," *Sens. Actuators A, Phys.*, vol. 85, nos. 1–3, pp. 147–152, Aug. 2000, [Online]. Available: https://www.sciencedirect.com/science/article/pii/S092442470000385X

[51] T. Ishihara, K. Suzuki, S. Suwazono, M. Hirata, and H. Tanigawa, "CMOS integrated silicon pressure sensor," *IEEE J. Solid-State Circuits*, vol. SSC-22, no. 2, pp. 151–156, Apr. 1987.

[52] S. Ren, W. Yuan, D. Qiao, J. Deng, and X. Sun, "A micromachined pressure sensor with integrated resonator operating at atmospheric pressure," *Sensors*, vol. 13, no. 12, pp. 17006–17024, Dec. 2013.

[53] S. Banerji, "Development of system-on-chip CMOS-MEMS pressure sensors," Ph.D. dissertation, Universitat Politècnica de Catalunya, Barcelona, Spain, 2017.

[54] M. I. Younis, *MEMS Linear and Nonlinear Statics and Dynamics*. New York, NY, USA: Springer, 2011, doi: 10.1007/978-1-4419-6020-7.
[55] S. Banerji, D. Fernandez, and J. Madrenas, "A comprehensive high-level model for CMOS-MEMS resonators," *IEEE Sensors J.*, vol. 18, no. 7, pp. 2632–2640, Apr. 2018. [Online]. Available: http://ieeexplore.ieee.org/document/8268083/
[56] B. Kim et al., "Temperature dependence of quality factor in MEMS resonators," in *J. Microelectromech. Syst.*, vol. 17, no. 3, pp. 755–766, Jun. 2008.
[57] S. Banerji, J. Madrenas, and D. Fernandez, "Temperature and pressure characterization of the quality factor in a CMOS-MEMS resonator," in *Proc. IEEE SENSORS*, Orlando, FL, USA, Oct. 2016, pp. 1–3. [Online]. Available: http://ieeexplore.ieee.org/document/7808403/
[58] V. Kaajakari. *MEMS Tutorial: Pull-in Voltage in Electrostatic Microactuators*. Accessed: Dec. 7, 2022. [Online]. Available: http://www.kaajakari.net/%7Eville/research/tutorials/pull_in_tutorial.pdf
[59] V. Kaajakari. *MEMS Tutorial: Nonlinearity in Micromechanical Resonators*. Accessed: Dec. 7, 2022. [Online]. Available: http://www.kaajakari.net/%7Eville/research/tutorials/nonlinear_resonators_tutorial.pdf
[60] V. Kaajakari. *MEMS Tutorial: Mechanical Noise in Microelectro mechanical Systems*. Accessed: Dec. 7, 2022. [Online]. Available: http://www.kaajakari.net/ville/research/tutorials/mech_noise_tutorial.pdf
[61] S. Banerji, P. Michalik, D. Fernández, J. Madrenas, A. Mola, and J. Montanyà, "CMOS-MEMS resonant pressure sensors: Optimization and validation through comparative analysis," *Microsyst. Technol.*, vol. 23, no. 9, pp. 3909–3925, Sep. 2017, doi: 10.1007/s00542-016-2878-3.
[62] J. Lenz and A. S. Edelstein, "Magnetic sensors and their applications," *IEEE Sensors J.*, vol. 6, no. 3, pp. 631–649, Jun. 2006.
[63] A. Chulliat et al. (2020). *The U.S./U.K. World Magnetic Model for 2020–2025: Technical Report*. [Online]. Available: https://repository.library.noaa.gov/view/noaa/24390
[64] R. S. Popovic, Z. Randjelovic, and D. Manic, "Integrated Hall-effect magnetic sensors," *Sens. Actuators A, Phys.*, vol. 91, nos. 1–2, pp. 46–50, Jun. 2001. [Online]. Available: http://www.sciencedirect.com/science/article/pii/S0924424701004782
[65] *Asahi Kasei AK09916C 3-Axis Electronic Compass IC Datasheet*, Asahi Kasei Corp., Tokyo, Japan, Dec. 2015.
[66] F. Primdahl, "The fluxgate magnetometer," *J. Phys. E, Sci. Instrum.*, vol. 12, no. 4, p. 241, 1979. [Online]. Available: http://stacks.iop.org/0022-3735/12/i=4/a=001
[67] (2011). *Bosch Sensortec BMC050 Compass Product Page*. [Online]. Available: https://www.bosch-sensortec.com/bst/products/all_products/bmc050
[68] T. McGuire and R. Potter, "Anisotropic magnetoresistance in ferromagnetic 3D alloys," *IEEE Trans. Magn.*, vol. M-11, no. 4, pp. 1018–1038, Jul. 1975.
[69] (2013). *MEMSIC Magnetic Sensors Product Catalog*. [Online]. Available: http://www.memsic.com/magnetic-sensors
[70] R. Ferreira, E. Paz, P. P. Freitas, J. Ribeiro, J. Germano, and L. Sousa, "2-axis magnetometers based on full wheatstone bridges incorporating magnetic tunnel junctions connected in series," *IEEE Trans. Magn.*, vol. 48, no. 11, pp. 4107–4110, Nov. 2012.
[71] (2013). *Freescale MAG3110 3-Axis Electronic Compass Datasheet*. [Online]. Available: http://www.nxp.com/assets/documents/data/en/data-sheets/MAG3110.pdf
[72] M. Li, V. T. Rouf, M. J. Thompson, and D. A. Horsley, "Three-axis Lorentz-force magnetic sensor for electronic compass applications," *J. Microelectromech. Syst.*, vol. 21, no. 4, pp. 1002–1010, Aug. 2012.
[73] M. Li et al., "Single-structure 3-axis Lorentz force magnetometer with sub-30 nT/$\sqrt{}$ HZ resolution," in *Proc. IEEE 27th Int. Conf. Micro Electro Mech. Syst. (MEMS)*, Jan. 2014, pp. 80–83.
[74] V. Kumar, A. Ramezany, M. Mahdavi, and S. Pourkamali, "Amplitude modulated Lorentz force MEMS magnetometer with picotesla sensitivity," *J. Micromech. Microeng.*, vol. 26, no. 10, Sep. 2016, Art. no. 105021, doi: 10.1088/0960-1317/26/10/105021.
[75] T. Bakke, J. Schmidt, M. Friedrichs, and B. Völker, "Etch stop materials for release by vapor HF etching," in *Proc. Micromech. Eur. Workshop*, vol. 122, 2005, pp. 103–106.
[76] C. H. Tsau and T. K. Nunan, "Silicon-rich nitride etch stop layer for vapor HF etching in MEMS device fabrication," U.S. patent 12 813 117, Jun. 10, 2010.
[77] J. M. Sanchez-Chiva, J. Valle, D. Fernandez, and J. Madrenas, "A mixed-signal control system for Lorentz-force resonant MEMS magnetometers," *IEEE Sensors J.*, vol. 19, no. 17, pp. 7479–7488, Sep. 2019. [Online]. Available: https://ieeexplore.ieee.org/document/8701467
[78] J. M. Sanchez-Chiva, J. Valle, D. Fernandez, and J. Madrenas, "A test setup for the characterization of Lorentz-force MEMS magnetometers," *IEEE Open J. Circuits Syst.*, vol. 2, pp. 587–596, 2021. [Online]. Available: https://ieeexplore.ieee.org/document/9536262
[79] SPTS. (2019). *Introduction to HF Vapor Etch*. [Online]. Available: https://www.spts.com/assets/media/hf-intro-a4-02-09-2019.pdf
[80] R. Doering and Y. Nishi, *Handbook of Semiconductor Manufacturing Technology*, 2nd ed. Boca Raton, FL, USA: CRC Press, 2017, doi: 10.1201/9781420017663.
[81] Memsstar. (2022). *Vapor HF (Hydrogen Fluoride) Etching*. [Online]. Available: https://memsstar.com/mems-tools/vapor-hf-etching/
[82] A. Shilov. (2020). *TSMC's Estimated Wafer Prices Revealed*. [Online]. Available: https://www.tomshardware.com/news/tsmcs-wafer-prices-revealed-300mm-wafer-at-5nm-is-nearly-dollar17000
[83] J. H. Lau, *Semiconductor Advanced Packaging*. Singapore: Springer, 2021, doi: 10.1007/978-981-16-1376-0.

Daniel Fernández received the M.Sc. degree in telecommunication engineering in 2004, the Ph.D. degree in 2008, and the M.B.A. degree in 2009.

He is currently working in the area of ultralow-power, energy-harvesting wireless remote identification and sensing integrated circuits and leads a microelectronics design team of six analog and digital engineers within the company from the Universitat Politècnica de Catalunya (UPC). From 2008 to 2010, he worked as a Postdoctoral Researcher at the Department of Electronic Engineering, Universitat Politècnica de Catalunya (UPC), Barcelona, Spain, in the fields of CMOS surface micromachining, circuits and control architectures for microelectromechanical system (MEMS) sensors and actuators, translinear circuits for analog signal processing, and integrated power converters. From 2010 to 2014, he worked as a Principal ASIC Engineer at Baolab Microsystems, Barcelona, where he developed circuits and architectures for CMOS MEMS/NEMS-based products, and as an ASIC Design Engineer Contractor for the European Space Agency designing radiation-hardened integrated circuits and interface blocks for space exploration in interplanetary missions. In 2014, he co-founded Nanusens, Barcelona, a deep-tech start-up company dedicated to CMOS-MEMS design, where he served until 2020 as its Chief Technology and Science Officer by leading teams up to seven researchers and several subcontracted companies, and managing research and development projects up to 3 M€ budgets. From 2020 to 2021 he was a Senior Researcher Engineer at the Institut de Física d'Altes Energies (IFAE), Barcelona, where he developed innovative integrated circuits for medical implants. He is the Microelectronics Director of Wiyo Technologies, Alcobendas, Spain.

Piotr Michalik was born in Łódź, Poland, in 1984. He received the master's degree in electronics engineering from the Łódź University of Technology, Łódź, in 2008, and the Ph.D. (cum laude) degree from the Universitat Politècnica de Catalunya, Barcelona, Spain, in 2015.

From 2007 to 2010, he was with the Łódź University of Technology, where he developed bioinspired dynamically reconfigurable digital VLSI circuits and digital-intensive micro-electromechanical system (MEMS) interfaces. From 2016 to 2020, he worked at Nanusens, Barcelona, as a Principal MEMS and ASIC Design Engineer developing CMOS-MEMS motion sensors targeted for high-volume CMOS processes. Since 2020, he has been the Analog/RF IC Design Coordinator at Wiyo Technologies, Alcobendas, Spain. From 2010 to 2014, he was the Spanish Ministry of Education FPU Doctoral Scholarship Holder at the Universitat Politècnica de Catalunya, where he worked on novel CMOS-MEMS acceleration sensors, time-to-digital converters for light detection and ranging (LiDAR), as well as on radiation-hardened integrated circuits for the European Space Agency-funded projects. In 2015, his research on CMOS-MEMS accelerometers was awarded with Catalan government funded "Llavor grant for innovative projects with the potential for being incorporated into the production sector" and concluded with filing and licensing out an international patent. In 2016, he was doing an RF HW design consulting for Indra Systems, Barcelona.

Juan Valle received the dual M.Sc. degrees in physics, industrial engineering from University Alfonso X el Sabio (UAX), Madrid, Spain, in 2000 and 2002, respectively, and the Ph.D. degree in electrical engineering from Universitat Politécnica de Catalunya (UPC), Barcelona, Spain, in 2022.

He is a Principal MEMS Engineer at SiTime, Rijswijk, The Netherlands. He is working in the field of timing devices, more specifically, micro-electromechanical system (MEMS) resonators and their productization. From 2001 to 2002, he worked as a Microsystems and Nanotechnology Consultant at the National Institute for Aerospace Technology (INTA), Madrid. He specialized in multiphysics simulations before joining Delphi Diesel Systems, Stonehouse, U.K., as an Analyst Engineer in 2004. In 2005, he joined Baolab Microsystems, Barcelona, where he researched on the fields of MEMS sensors and micromanufacturing processes for nine years, where he filed ten patent applications on related fields. He devised design techniques applicable to the MEMS fabrication inside the CMOS BEOL. Using these techniques, the first CMOS-MEMS three-axis magnetometer aimed at mass production was developed.

Saoni Banerji received the M.Sc. degree in electronics from Nanyang Technological University (NTU), Singapore, in 2014, and the Ph.D. degree in electronics engineering from the Universitat Politècnica de Catalunya (UPC), Barcelona, Spain, in 2017, with an FI AGAUR Grant from the Catalonian government in the fields of micro-electromechanical system (MEMS) design and circuits and designing control architectures for MEMS sensor signal conditioning.

After her Ph.D. degree, she worked in a CMOS-MEMS startup, Nanusens, Barcelona, as a Simulation and Characterization Engineer, from 2017 to 2018. In 2018, she joined the University of Tartu, Tartu, Estonia, as a Research Fellow of Microfabrication and Microtechnology, where she works toward designing and characterizing microsystems by integrating CMOS electronics with ionic electroactive polymer (IEAP) sensors dedicated to medical technologies. Her current research interests and competencies include integrating electronics in soft fiber sensors and actuators dedicated to medical and wearable applications, MEMS modeling, design of signal-conditioning architectures with CMOS processes, and testing and characterization of CMOS-MEMS devices.

Josep Maria Sánchez-Chiva was born in Barcelona, Spain, in 1989. He received the B.Sc. degree in telecommunication engineering and the M.Sc. and Ph.D. degrees in electronic engineering from the Universitat Politècnica de Catalunya, Barcelona, in 2011, 2014, and 2020, respectively.

During his thesis, he designed CMOS-micro-electromechanical system (MEMS) Lorentz-force magnetometers and their readout circuits and architectures. From 2012 to 2013, he was an Analog Design Intern with Broadcom Inc., Barcelona, where he worked in sigma–delta analog-to-converters (ADCs). From 2018 to 2020, he worked as an ASIC Design Engineer at Nanusens, Barcelona, where he designed circuits for the signal readout of monolithic CMOS-MEMS accelerometers. From 2020 to 2021, he worked as a Postdoctoral Researcher at the LIP6, Sorbonne Université, Paris, France, developing integrated power management circuits for remote-powered implants. From 2021 to 2022, he was a Postdoctoral Researcher at the Omega Microelectronics Center, Palaiseau, France, and Weeroc SAS working in integrated circuits for space applications and single-photon detection, Villebon-sur-Yvette, France. He is currently a Postdoctoral Researcher at GeePs research group (Sorbonne Université and CentraleSupélec, Gif-sur-Yvette, France), where he is working in the development of integrated circuits for piezoelectric transducers energy extraction to remotely power biomedical implants.

Jordi Madrenas received the M.Sc. degree in telecommunication engineering and the Ph.D. degree from the Universitat Politècnica de Catalunya (UPC), Barcelona, Spain, in 1986 and 1991, respectively.

He is a Professor with the Department of Electronics Engineering, UPC. He coordinates the Intelligent Sensors and Integrated Systems (IS2) Research Group. From 2000 to 2003, he was the Vice Dean of Studies with the Telecommunication Engineering School of Barcelona, UPC. He has participated in five European projects and he has coordinated nine Spanish national research projects and several contracts with companies. He currently leads a national project on low-power CMOS-compatible sensors with efficient bioinspired edge processing. He has coauthored 45 scientific journal articles, more than 150 international conference papers, two books, and six book chapters. He holds one international patent. His current research interests include analog, mixed-signal, and digital VLSI and field-programmable gate array (FPGA) design; CMOS-micro-electromechanical system (MEMS) design and conditioning; ultralow-power design; and bioinspired/neuromorphic system implementation.